Journal of Quantitative Spectroscopy & Radiative Transfer 218 (2018) 21–37

Contents lists available at ScienceDirect

Journal of Quantitative Spectroscopy & Radiative Transfer

journal homepage: www.elsevier.com/locate/jqsrt

Directional Polarimetric Camera (DPC): Monitoring aerosol spectral optical properties over land from satellite observation

Zhengqiang Li[a], Weizhen Hou[a,*], Jin Hong[b], Fengxun Zheng[a], Donggen Luo[b], Jun Wang[c], Xingfa Gu[a], Yanli Qiao[b]

[a] State Environment Protection Key Laboratory of Satellite Remote Sensing, Institute of Remote Sensing and Digital Earth, Chinese Academy of Sciences, Beijing 100101, China

[b] Key Laboratory of Optical Calibration and Characterization, Anhui Institute of Optics and Fine Mechanics, Chinese Academy of Sciences, Hefei 230031, China

[c] Department of Chemical and Biochemical Engineering, Center of Global and Regional Environmental Studies, and Informatics Initiative, University of Iowa, 4133 Seamans Center, Iowa City, IA 52242, USA

ARTICLE INFO

Article history:
Received 12 April 2018
Revised 1 June 2018
Accepted 5 July 2018
Available online 7 July 2018

Keywords:
Directional Polarimetric Camera (DPC)
GaoFen-5 satellite
Spectral aerosol optical depth (AOD)
Improved BRDF model
Inversion capability analysis

ABSTRACT

The Directional Polarimetric Camera (DPC) is the first Chinese multi-angle polarized earth observation satellite sensor, which will be launched onboard the GaoFen-5 Satellite in Chinese High-resolution Earth Observation Program. GaoFen-5 runs in a sun-synchronous orbit with an inclination angle of 98°, with the 13:30 PM local overpass time and the 2-days revisiting period. DPC employed a charge coupled device detection unit with 512×512 effective pixels from the 544×512 useful pixels, realizing spatial resolution of 3.3 km under a swath width of 1850 km. Meanwhile, DPC has 3 polarized channels (490, 670 and 865 nm) together with 5 non-polarized bands (443, 565, 763, 765 and 910 nm), and can obtain at least 9 viewing angles by continuously capturing series images over the same target on orbit. Based on the optimal estimation theory and improved bidirectional reflectance distribution function model, an inversion framework for the simultaneous retrieval of aerosol and surface parameters is presented by taking full advantage of available radiometric and polarimetric measurements. The retrieved wavelength-independent fine-mode and coarse-mode aerosol volumes are used to assess the DPC performance on the inversion capability of spectral aerosol optical depth (AOD), from which the Angstrom exponent and fine-mode fraction (FMF) could be further obtained. In addition, based on the synthetic DPC data for various observation geometries, aerosols and surface types, the aerosol inversion capabilities are systematically evaluated, and the information content analysis results show that the aerosol spectral optical properties can be well retrieved over various land surfaces.

1. Introduction

Aerosol is an important component of the global atmosphere and has a significant impact on climate change, air pollution, material transport, and ecological assessment. For example, while most aerosol particles reflect sunlight and cause a cooling effect, particulate matter such as black carbon absorbs solar radiation and causes atmospheric heating [1]. The aerosol components, such as black carbon deposited on ice and snow, further accelerate the ablation of ice and snow, and generate feedback-coupling effect between the cryosphere, hydrosphere, and radiation circle in the polar region [2]. These complex effects make aerosols, including their cloud effects, become the most important factor affecting the uncertainties in the climate change assessment [3]. On the other hand, aerosols with aerodynamic diameters of less than 2.5 μm ($PM_{2.5}$) have become the focus of attention for atmospheric pollution, because they can enter the people's lung with breathing and affect vital systems such as blood circulation [4,5]. The World Health Organization has estimated that there are more than 7 million people deaths directly and indirectly due to $PM_{2.5}$ pollution in the world each year [6,7]. Most aerosols have the universal characteristics including regional distribution of sources, variability of properties and short lifetime. For example, seasonal meteorological conditions can determine the transportation of aerosols from their sources and the vertical distributions through the atmosphere. While during the transport by the dry or deposition, in-cloud processes and atmospheric chemical reactions, the aerosol properties can be further modified [8]. Therefore, it is very important to obtain spatial distribution of aerosol parameters in large-

* Corresponding author.
E-mail address: houwz@radi.ac.cn (W. Hou).

https://doi.org/10.1016/j.jqsrt.2018.07.003
0022-4073/

scale and even global scales based on the satellite remote sensing [9].

Early aerosol satellite remote sensing was developed as a by-produce of atmospheric correction of the land surface signals, e.g., the Advanced Very High Resolution Radiometer (AVHRR) that began in the 1980s [10]. Due to the limitations such as the detection ability of its spectral channels, only the spatial distribution of aerosol optical loadings on the ocean was mainly obtained [11–13]. After recognizing the importance of satellite remote sensing of aerosols, and analyzing the related key technologies, such as the pioneering work of Kaufman et al. [14] on the decoupling of surface-atmosphere based on the dark targets dense vegetation, National Aeronautics and Space (NASA) has developed the modern aerosol satellite sensors represented by Moderate Resolution Imaging Spectroradiometer (MODIS) [15]. Since the year of 2000, continuous and daily revisited aerosol optical depth (AOD) monitoring results have been obtained over the land surface (mainly the dark surface, e.g. forest), thus greatly support the need of various fields for the regional aerosol information acquisition [16–19]. Subsequently, in order to address the limitations of dark targets surface, different approaches have been developed for the extending of surface applicability, such as the Deep Blue (DB) method can be used for the bright surface partially based on a priori surface reflectance library [20,21], and the AOD inversion methods for the Along Track Scanning Radiometers (ATSR) [22–25] and Multi-angle Imaging SpectroRadiometer (MISR) [26–28], based on the multi-angle detections. Although these methods and sensors solve the problem of surface applicability to a certain degree, there still have some limitations in the detection accuracy and the type of aerosol parameters obtained, such as the lack of key parameters to represent the size of aerosol particles [29].

From the theory [30] and ground testing [31], it has been proved that the polarimetric remote sensing can effectively improve the remote sensing accuracy of aerosols and have the ability to acquire the additional parameters [32]. Based on the airborne research [33], the University of Lille in France developed the multi-angle polarization imaging sensor Polarization and Directionality of the Earth's Reflectances (POLDER) with the support of the Centre National d'Etudes Spatiales (CNES), and launched 3 payloads on the Advanced Earth Observing Satellite (ADEOS)-1, 2 and the Polarization and Anisotropy of Reflectances for Atmospheric science coupled with Observations from a Lidar (PARASOL) satellite, respectively [34–36]. In particular, the global long-term sequences of multi-angle polarization datasets were obtained by the PARASOL from the year of 2004 to 2013. By developing the corresponding algorithms, many research breakthroughs have been made, such as the multi-parameter inversion of aerosols on the ocean [34,37], the inversion of fine aerosols over land [35,36], and the observations of the interaction between clouds and aerosols [38]. In recent years, with the progress of statistical optimization methods [39,40] and polarized surface models [41–44], a new generation of multi-parameter POLDER inversion method has basically matured and applied to the reprocessing of POLDER historical data.

In response to the urgent needs of atmospheric pollution issues and climate change assessment, based on the POLDER technology, the Anhui Institute of Optics and Fine Mechanics (AIOFM) Chinese Academy of Sciences, has developed a Directional Polarimetric Camera (DPC) space-borne sensor supported by the National Space Administration of China, with highlights of one time increase in spatial resolution (from about 6 $\times$ 7 km to 3.3 $\times$ 3.3 km) [45]. The first DPC sensor will be launched at May of 2018 with the Chinese atmospheric environment flagship satellite GaoFen-5 (GF-5) in the Chinese High-resolution Earth Observation System (CHEOS) program. Its main scientific goal is to obtain spectrally resolved aerosol optical parameters including spectral AOD ($\tau_a(\lambda)$), Angstrom exponent (α) and fine-mode fraction (FMF), and the relevant cloud and water vapor parameters, to support the environmental applications such as the atmospheric particulate pollution monitoring and climate effect assessment.

For this scientific goal, it is necessary to carry out the evaluation of the inversion capability of DPC aerosol key parameters based on a new generation of optimized inversion framework.

In response to this requirement, this paper firstly introduced the parameters and configuration of the DPC sensor in Section 2, then established the forward and inversion models, and further introduced the inversion capability assessment method based on the information content in Section 3. After that, the test setup for different seasons, observation conditions, surface and aerosol models are presented in Section 4. Subsequently, a complete DPC inversion capability assessment is given in Section 5, and supplemented discussion was made on the influences of loading variation, other retrieved aerosol paraters and aerosols model errors in Section 6. Finally, we get the conclusion of our work in Section 7.

2. The DPC sensor onboard GF-5 satellite

From May 2010, China has launched the construction of the Chinese High-resolution Earth Observation System (CHEOS) program. As a major project, CHEOS focuses on building a new Earth observation system with high spatial, temporal and spectral resolution, to achieve all-weather, all-day and global coverage observation capability, and thus further to provide operational applications and services in the various fields, such as agriculture, disaster, resource and environment [45]. The satellite series of CHEOS contain 7 satellites, which are named form GF-1 to GF-7 in sequence. Correspondingly, GF-1 and GF-2 are the high spatial resolution satellites [46,47], GF-3 is the high-resolution radar satellite [48], GF-4 is an optical geostationary satellite [49], GF-5 is a high spectral and atmospheric observation satellite, GF-6 is a multi-spectral satellite and GF-7 is a three-dimensional mapping satellite, respectively. Until to April 2018, the CHEOS project has successfully launched 4 satellites from GF-1 to GF-4.

As the flagship of the environment and atmosphere observation satellite in the CHEOS program, GF-5 will be launched in May 2018. There are six payloads onboard the GF-5 satellite, including Advanced Hyperspectral Imager (AHSI), Visual and Infrared Multispectral Sensor (VIMS) [50,51], Atmospheric Infrared Ultraspectral Senor (AIUS), Environment Monitoring Instrument (EMI) [52], Greenhouse-gases Monitoring Instrument (GMI) [53] and Directional Polarization Camera (DPC) [54,55], just as shown in Fig. 1(a). The GF-5 satellite runs in a sun-synchronous orbit with an inclination angle of 98°. The overpass local time is 13:30 PM and the design life is 8 years. The six sensors onboard GF-5 works together for environment monitoring and assessment, focusing on aerosols, gas-house gases, polluted gases, cloud, water vapor, waste water, land surface, vegetation, biomass burning and urban environment, etc.

The Directional Polarimetric Camera (DPC) is the first Chinese multi-angle polarized earth observation satellite sensor, which is the type of POLDER polarimetric imager, as illustrated in Fig. 1(b). Before the spaceborne DPC instrument, China has tested polarimetric imager techniques in the TG-2 space laboratory lunched in September 2016. Immediately after that, China lunched TanSat on December 2016 for CO_2 monitoring which contains a Cloud and Aerosol Polarimetric Imager (CAPI). For observing the information of clouds and aerosols, CAPI has two polarimetric channels (670 and 1640 nm) working together with other 3 non-polarized channels, but without multi-angle observation features at all these channels [56]. The instrumental parameters of DPC on board GF-5 satellite are listed in Table 1. The DPC employed a charge coupled device (CCD) detection unit with 512 $\times$ 512 effective pixels from the

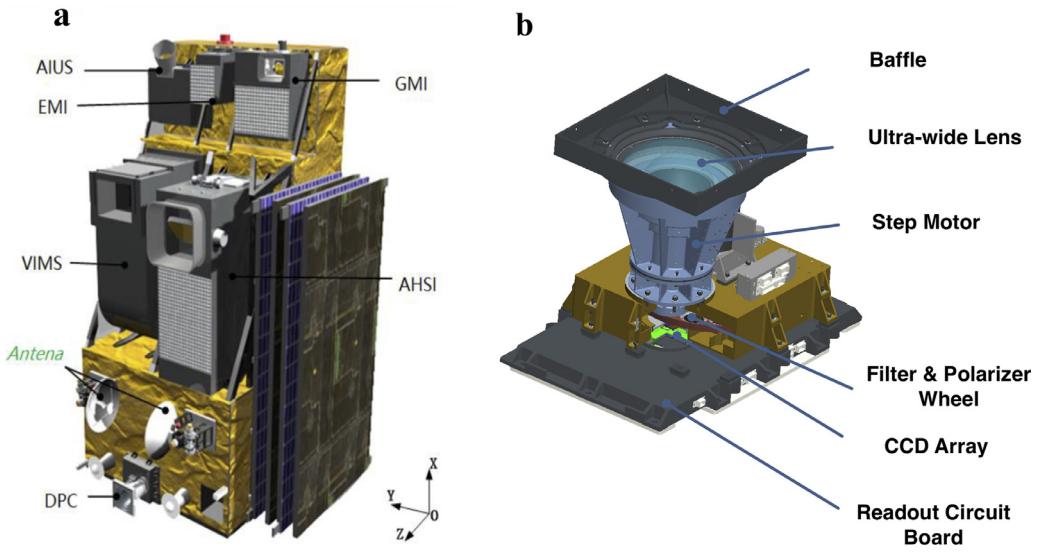

Fig. 1. Illustration of the GF-5 satellite (a) and the Directional Polarized Camera (b).

Table 1
The instrumental parameters of DPC sensor on board GF-5 satellite.

Parameter	Value	Parameter	Value
Instrument FOV	± 50° (across/along-track)	Polarized angle	0°, 60°, 120°
Spatial res. (km)	3.3	Stokes parameters	I, Q, U
Swath width (km)	1850	Rad. Cal. Error	≤ 5%
Multi-angle	≥ 9	Pol. Cal. Error	≤ 0.02
Image pixels	512 × 512	Band width (nm)	20, 20, 20, 20, 10, 40, 40, 20
Spectral band (nm): P for polarization	443, 490 (P), 565, 670 (P), 763, 765, 865 (P), 910		

544 × 512 useful pixels, realizing spatial resolution of 3.3 km under a swath width of 1850 km. The 2-days revisiting period allows it visiting the temporal variation of atmospheric pollution. The DPC has 3 polarized bands/wavelengths (490, 670 and 865 nm) together with 5 non-polarized bands (443, 565, 763, 765 and 910 nm). The polarizer and filters are installed in one wheel and thus obtaining spectral polarized measurements through wheel's quickly rotating. Meanwhile, the step motor rotates at a fixed angle each time, and then the measurement in different wavelength bands could be successively obtained [57]. The polarization and multi-angle measurement principles are illustrated in Sections 2.1 and 2.2, respectively. The spectral widths of 8 bands are from 10 to 40 nm. The radiometric and polarimetric calibration errors are less than about 5% and 0.02 (with respect to the degree of linear polarization, abbreviated as DOLP which is in a range of 0–1), respectively, which will be continuously maintained by performing on-orbit vicarious calibration combing laboratory calibration coefficients. DPC share many similarities in the instrument design with POLDER, the distinguishing feature is that the pixel spatial resolution of DPC (3.3 × 3.3 km) has significant improvement than POLDER (about 6 × 7 km), thus higher spatial resolution of aerosol and surface products could be further retrieved from the measurements of DPC.

2.1. The principle of polarimetric observation

DPC has 3 polarized bands (490, 670 and 865 nm) and each polarized band contains 3 polarized channels (0°, 60°, and 120°). By combining the three polarized channels, the Stokes vector (*I, Q, U*) of the electromagnetic field at the top-of-atmosphere (TOA) entering the Field-of-View (FOV) of satellite sensors can be obtained, which are measurements used to the retrieval of atmospheric parameters. As to each polarized band of DPC, by noting the radiometric measurement values at 3 polarized channels as $L_1 = 0°$, $L_2 = 60°$ and $L_3 = 120°$ respectively, we have

$$\begin{cases} L' = \frac{2}{3}(L_1 + L_2 + L_3) \\ L'_P = \frac{4}{3}\sqrt{L_1^2 + L_2^2 + L_3^2 - L_1L_2 - L_1L_3 - L_2L_3} \end{cases}, \quad (1)$$

where, L' is the entrance total radiance and L'_P the polarized radiance. Here, to clearly explain the expression in Eq. (1), as assuming a linear polarized light in the direction of the detector, we define that $S_0 = \frac{2}{3}(L_1 + L_2 + L_3)$, $S_1 = \frac{2}{3}(2L_1 - L_2 - L_3)$, $S_2 = \frac{2}{\sqrt{3}}(L_2 - L_3)$, and $S_3 = 0$, thus we can use the relationship $L' = S_0$ and $L'_P = \sqrt{S_1^2 + S_2^2}$. Usually, in order to obtain the required inputs of forward models (i.e. the radiative transfer model), we further have the normalized radiance & polarized radiance:

$$\begin{cases} L = L'/E_0 \\ L_P = L'_P/E_0 \end{cases}, \quad (2)$$

here L and L_P are the normalized radiance and polarized radiance, and E_0 is the extraterrestrial solar irradiance. Moreover, the well-known Degree of Linear Polarization is defined as $DOLP = L_P/L$. On the basis of these measurements, we can calculate the normalized Stokes parameters:

$$\begin{cases} I = L \\ Q = L_P\cos(2\varphi) \\ U = L_P\sin(2\varphi) \end{cases}, \quad (3)$$

where, *I, Q* and *U* are referred to the axes linked to the meridian plane which contains the viewing direction. Besides, φ is the angle between the polarization direction and meridian plane, which need to be calculated based on geometric parameters and laboratory calibration parameters. Based on the results of *Q* and *U*, we can further have $L_P = \sqrt{Q^2 + U^2}$.

It should be noted, the actual radiometric and polarimetric registration/calibration of DPC measurements are much more complex due to the ultra-wide FOV imaging mechanism [58], and here we

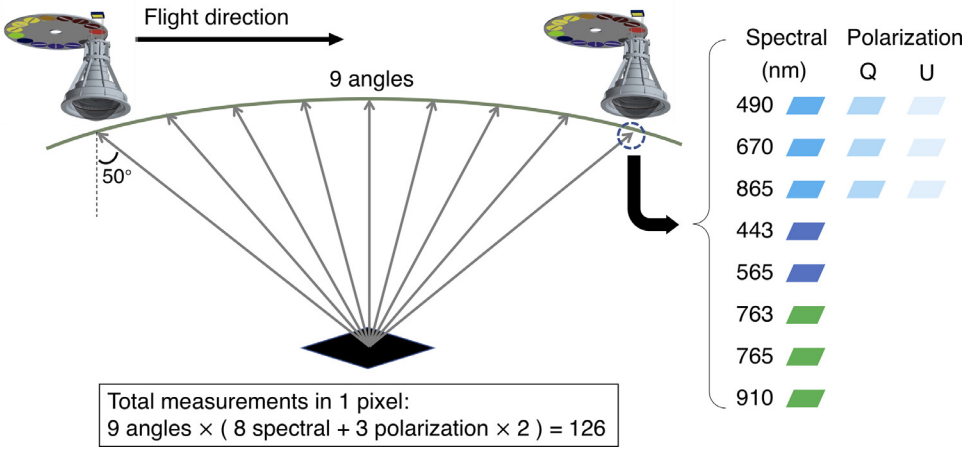

Fig. 2. By taking the measurements with 9 viewing angles as an example, the multi-angle observation principle and the description of measurement dataset of DPC are described. The color scales associated to the spectral channels on the right are employed to distinguish the 3 polarized bands (490, 670, 865 nm) and 5 non-polarized bands (443, 565, 763, 765, 910 nm), in which the 443 and 565 nm bands can be used together with 3 polarized bands for aerosol retrieval, the 763 and 765 nm bands are for cloud pressure detection in Oxygen A band, and the 910 nm band is for water vapor retrieval.

are mainly focusing on providing definitions and physical meaning expression. The DPC design has wedges on the polarisers (as POLDER) which improves the registration of the polarized acquisitions, but only for the area around nadir.

2.2. The principle of multi-angle observation

Based on the ultra-wide (100°) FOV and the continuous imaging capability with the satellite platform movements, the DPC can obtain multi-angle viewing of one surface targets in more than 9 directions, which forms an observation vector containing at least 126 measurements at each pixel (see Fig. 2). This multi-angle capability depends on several aspects, including the satellite orbit, flying speed, sensor FOV and CCD parameters. The DPC reference grid is based on the sinusoidal equal area projection with an equidistant grid (3.3 × 3.3 km), which is similar as POLDER/PARASOL but with higher resolution [59]. Correspondingly, the projection step is constant along a meridian with a resolution of about 0.0295°. Indeed, there is an advantage to work on this product, which is to minimize the effect on the edge of the FOV. Fig. 2 shows a simple illustration on the multi-angle observation. For the purpose of aerosol retrieval, the major information can be used comes from 3 polarized bands plus 2 non-polarized bands (443, 565 nm) and thus the corresponding observing vector contains at least 99 measurements. These sufficient measurements provide a mathematic potential for the simultaneously determining complex aerosol parameters, e.g. spectral AOD instead of previous satellite retrieval products of AOD at single wavelength (e.g. that of MODIS).

3. Retrieval method based on Optimal Estimation Theory

3.1. Forward modeling

3.1.1. Aerosol model

For the aerosol model in the forward simulations, a bimodal lognormal function is used to describe the volume particulate size distribution of spherical aerosol particles with the combination of fine-mode and coarse-modes aerosols in the form of

$$\frac{dV}{d\ln r} = \frac{V_0^{\mathrm{f}}}{\sqrt{2\pi}\ln\sigma_g^{\mathrm{f}}}\exp\left[-\frac{\left(\ln r-\ln r_V^{\mathrm{f}}\right)}{2\ln^2\sigma_g^{\mathrm{f}}}\right] + \frac{V_0^{\mathrm{c}}}{\sqrt{2\pi}\ln\sigma_g^{\mathrm{c}}}\exp\left[-\frac{\left(\ln r-\ln r_V^{\mathrm{c}}\right)}{2\ln^2\sigma_g^{\mathrm{c}}}\right], \quad (3)$$

Where V is the particle volume, r is the radius, r_V represent the volume geometric median radius with unit of μm, σ_g represent the geometric standard deviation, and the superscript f and c are respectively for fine and coarse mode [60]. Clearly, the total aerosol volume (V_0 with unit of $\mu\mathrm{m}^3/\mu\mathrm{m}^{-2}$) is the sum of V_0^{f} and V_0^{c}, and the volume fine-mode fraction (FMF_V) can be obtained by V_0^{f}/V_0.

Besides, the effective radius r_{eff} and the effective variance v_{eff} can be converted from the geometric parameters by the relationship as [61]

$$\begin{cases} r_{\mathrm{eff}} = r_V \exp\left(-\frac{1}{2}\ln^2\sigma_g\right), \\ v_{\mathrm{eff}} = \exp\left(\ln^2\sigma_g\right) - 1 \end{cases} \quad (4)$$

and in this study, we consider using r_{eff} and v_{eff} as the input in the forward simulation.

Consequently, the AOD at each wavelength could be derived from the columnar volume concentration as

$$\tau_{\mathrm{a}}(\lambda) = \tau_{\mathrm{a}}^{\mathrm{f}}(\lambda) + \tau_{\mathrm{a}}^{\mathrm{c}}(\lambda) = \frac{3V_0^{\mathrm{f}}}{4r_{\mathrm{eff}}^{\mathrm{f}}}Q_{\mathrm{ext}}^{\mathrm{f}}(\lambda) + \frac{3V_0^{\mathrm{c}}}{4r_{\mathrm{eff}}^{\mathrm{c}}}Q_{\mathrm{ext}}^{\mathrm{c}}(\lambda), \quad (5)$$

where Q_{ext} means the extinction efficiency factor, which is equal to the ratio of extinction cross section to geometric cross section, $\tau_{\mathrm{a}}^{\mathrm{f}}$ and $\tau_{\mathrm{a}}^{\mathrm{c}}$ represent the fine-mode and coarse-mode AOD, respectively [62]. Correspondingly, the Angstrom exponent (α) [63] and fine-mode fraction (FMF) of AOD [64,65] can be calculated by

$$\alpha = \ln\frac{\tau_{\mathrm{a}}(\lambda_{\mathrm{p}})}{\tau_{\mathrm{a}}(\lambda_{\mathrm{q}})} / \ln\frac{\lambda_{\mathrm{q}}}{\lambda_{\mathrm{p}}}, \quad (6)$$

$$\mathrm{FMF}\ (\lambda) = \tau_{\mathrm{a}}^{\mathrm{f}}(\lambda)\ /\tau_{\mathrm{a}}(\lambda), \quad (7)$$

where, λ_{p} and λ_{q} in Eq. (6) are usually chosen for special wavelength pairs, e.g. 490 and 865 nm. For the case of DPC, the number of λ can be used in the aerosol retrieval is up to 5, the assessment of retrieval performance for AOD, FMF and α on all these wavelengths together might be complex and not explicit. Fortunately, we noticed that all these aerosol spectral optical parameters result from V_0^{f} and V_0^{c} following above derivation. In this paper, therefore, the wavelength-independent V_0^{f} and V_0^{c} are employed in the forward simulations and inversion framework in instead of varied AOD and FMF along the wavelength. This treatment will make our analysis more explicit and the validity in the meaning of information content analysis has been approved in the previous works [60,61]. More details can also be found in Section 5.3.

3.1.2. Surface model

For the surface reflectance model, the land surface reflectance matrix $\boldsymbol{R}$ can be represented as a sum of surface reflection phenomena for intensity and polarization as [39]

$$\boldsymbol{R}(\mu_0, \mu_v, \phi, \lambda) = r_\lambda \begin{bmatrix} 1 & 0 & 0 & 0 \\ 0 & 0 & 0 & 0 \\ 0 & 0 & 0 & 0 \\ 0 & 0 & 0 & 0 \end{bmatrix} + \rho_{\text{Maignan}} \mathbf{F}(\gamma, n_i), \quad (8)$$

with the empirical coefficient

$$\rho_{\text{Maignan}} = \frac{C \exp(\tan\gamma) \exp(\text{NDVI})}{4(\mu_0 + \mu_v)}, \quad (9)$$

where μ_0 and μ_v represent the cosine of solar zenith angles and viewing zenith angle respectively, ϕ represents the relative azimuth angle defined by the solar azimuth angles ϕ_0 and viewing azimuth angle ϕ_v, r_λ represent the bidirectional reflectance distribution function (BRDF) at the wavelength of λ, $\mathbf{F}(\gamma, n_i)$ means the Fresnel reflection matrix, n_i is the reflective index of the vegetative matter, γ means the half the phase angle, which is supplementary to the scattering angle. While in formulation of Eq. (9), NDVI means the normalized difference vegetation index, and can be obtained by two surface reflectance at two wavelength (e.g. one visible and one infrared wavelength band); C is the only free linear parameter in Eq. (9), and the value depends on the surface type [42].

For the contribution of surface polarized reflectance, the bidirectional polarized reflectance distribution function (BPDF) can be represented in the form as

$$R_p^s(\mu_0, \mu_v, \phi) = \rho_{\text{Maignan}} \mathbf{F}_{1,2}(\gamma, n_i), \quad (10)$$

where $\mathbf{F}_{1,2}(\gamma, n_i)$ represent the polarized component of the $\mathbf{F}(\gamma, n_i)$. Because the surface-polarized reflectance can be regarded as independent on the wavelength [66], we only need to consider one variable parameter C for BPDF model with corresponding NDVI in the forward simulation. While for the contribution of surface reflectance of multi-angle observations, we will discuss with the improved BRDF model in the following subsection.

3.1.3. The improved BRDF model

The kernel-driven Ross–Li BRDF model for surface reflectance can be presented as

$$r_\lambda(\mu_0, \mu_v, \phi) = f_{\text{iso}}(\lambda) + k_1(\lambda) f_{\text{geom}}(\mu_0, \mu_v, \phi) + k_2(\lambda) f_{\text{vol}}(\mu_0, \mu_v, \phi), \quad (11)$$

where f_{iso}, f_{geom} and f_{vol}, respectively represent isotropic, geometric-optical and volumetric surface scattering, and $f_{\text{iso}}(\lambda)$, $k_1(\lambda)$ and $k_2(\lambda)$ are the coefficients of the BRDF kernels at the wavelength λ. Correspondingly, in this study the Ross-thick kernel is used as $f_{\text{vol}}(\mu_0, \mu_v, \phi)$ [67], and Li-sparse kernel is used for the description of $f_{\text{geom}}(\mu_0, \mu_v, \phi)$ [68,69].

Because these three coefficients in Eq. (11) vary with the wavelength, to make the inversion framework easier and simpler, we follow the way of rewritten formulas as

$$r_\lambda(\mu_0, \mu_v, \phi) = f(\lambda)[1 + k_1 f_{\text{geom}}(\mu_0, \mu_v, \phi) + k_2 f_{\text{vol}}(\mu_0, \mu_v, \phi)], \quad (12)$$

where k_1 and k_2 represent the wavelength independent linear model parameters, and $f(\lambda)$ is the wavelength dependent model parameter [44]. Obviously, the number parameters in the improved BRDF model could be significantly decreased compared with the traditional Ross-Li BRDF model.

3.1.4. Vector radiative transfer model

For the vector radiative transfer model to simulate the synthetic measurement of DPC, we select UNified Linearized Vector Radiative Transfer Model (UNL-VRTM) as the forward model, which was specifically designed for the simulation of atmospheric remote sensing observations and for the inversion of aerosol, gas, cloud, and/or surface properties from these observations [70]. Several modules including the VLIDORT for radiative transfer [71], a linearized Mie and a linearized T-Matrix code for aerosol single scattering [72], a Rayleigh scattering module, and line-by-line gas absorption calculation with HITRAN database are comprised in UNL-VRTM. Meanwhile, some optional BRDF [73] and BPDF [42] models are also integrated to characterize the surface properties. The outputs, not only include the full elements of the Stokes vector, but also contain their sensitivities (Jacobians) with respect to various parameters relevant to aerosol microphysics and optical property, gas absorption, and surface properties. UNL-VRTM has also been used to study the information content and develop the inversion algorithm for retrieval of aerosol and surface properties from the ground, airborne and space-borne measurements [61,74–79]. Moreover, for the Jacobians of Stoker vector with respect to the parameters of improved BRDF, the results have been validated with the finite difference method [77].

3.2. Inversion modeling

3.2.1. Inversion framework

Based on the OE theory [80], the forward model can be defined in the form as

$$\mathbf{y} = \mathbf{F}(\mathbf{x}) + \boldsymbol{\epsilon}, \quad (13)$$

where $\mathbf{x}$ represents a state vector that contains n parameters to be retrieved, $\mathbf{y}$ represents an observation vector with m elements of measurements, $\mathbf{F}$ means a forward model that describes the physical relationship of how $\mathbf{y}$ and $\mathbf{x}$, and $\boldsymbol{\epsilon}$ means an experimental error term that includes observation noise and forward modeling uncertainty.

Following the optimal estimation theory, the scalar-valued cost function $J(\mathbf{x})$ used for inversion can be written as [66,81,82]:

$$J(\mathbf{x}) = \frac{1}{2}[\mathbf{y} - \mathbf{F}(\mathbf{x})]^T \mathbf{S}_\epsilon^{-1} [\mathbf{y} - \mathbf{F}(\mathbf{x})] + \frac{1}{2}(\mathbf{x} - \mathbf{x}_a)^T \mathbf{S}_a^{-1} (\mathbf{x} - \mathbf{x}_a), \quad (14)$$

where superscript "T" and "-1" represents the transpose operation and inverse operation of matrix, respectively, $\mathbf{S}_a$ means the error covariance matrix of the a priori estimate $\mathbf{x}_a$, $\mathbf{S}_\varepsilon$ means the covariance matrix of the observational error from both the measurements and the error prorogation in the forward model, and can be represented in the sum form of $\mathbf{S}_y$ and $\mathbf{K}_b\mathbf{S}_b\mathbf{K}_b^T$. Here $\mathbf{S}_y$ means the measurement error covariance matrix, $\mathbf{S}_b$ means the error covariance matrix for a vector $\mathbf{b}$ of forward model that are not contained in $\mathbf{x}$ but quantitatively influence the TOA stokes vector measurements, and $\mathbf{K}_b$ means the Jacobians matrix of measurements $\mathbf{y}$ with respect to the vector $\mathbf{b}$. In the optimized iteration, the gradient vector $\nabla_\mathbf{x} J(\mathbf{x})$ is used as the form of

$$\nabla_\mathbf{x} J(\mathbf{x}) = -\mathbf{K}^T \mathbf{S}_\epsilon^{-1} [\mathbf{y} - \mathbf{F}(\mathbf{x})] + \mathbf{S}_a^{-1} (\mathbf{x} - \mathbf{x}_a), \quad (15)$$

in which, the Jacobians matrix $\mathbf{K}$ means the partial derivatives of $\mathbf{F}(\mathbf{x})$ with respect to $\mathbf{x}$.

For the inversion model, the objective function will be optimized to the minimum result $\min J(\mathbf{x})$ subject to the conditional constraints [83–86].

3.2.2. Inversion setting

In this inversion framework, we define the state vector as

$$\mathbf{x} = \left[V_0^f,\ V_0^c,\ f(\lambda_1),\ \ldots,\ f(\lambda_5),\ k_1,\ k_2,\ C\right]^T, \quad (16)$$

which contains 2 parameters for the aerosols, 7 parameters for the improved BRDF model, and 1 parameter for the BPDF. Meanwhile, we have the aerosol model vector as

$$\mathbf{b} = \left[r_{\text{eff}}^{\text{f}},\ v_{\text{eff}}^{\text{f}},\ r_{\text{eff}}^{\text{c}},\ v_{\text{eff}}^{\text{c}},\ m_{\text{r}}^{\text{f}}(\lambda),\ m_{\text{i}}^{\text{f}}(\lambda),\ m_{\text{r}}^{\text{c}}(\lambda),\ m_{\text{i}}^{\text{c}}(\lambda) \right]^T, \tag{17}$$

here these parameters in the aerosol model vector **b** of forward model that are not contained in **x** but quantitatively influence the DPC measurements, where r_{eff} and v_{eff}, respectively represent the effective radius and the effective variance, $m_{\text{r}}(\lambda)$ and $m_{\text{i}}(\lambda)$, respectively represent the real and imaginary part of complex refractive index at the wavelength λ, and the superscript f and c represent the a fine and a coarse mode respectively.

For the forward simulations of synthetic data for DPC measurements, we consider 5 wavelength bands at the center of 443, 490 (P), 565, 670 (P), and 865 (P) nm, and correspondingly denote these wavelength form λ_1 to λ_5, in which λ_2, λ_4 and λ_5 represent the bands with polarimetric measurement, and λ_1 and λ_3 correspond to the bands only with scalar measurement. Consequently, the observational vector **y** can be defined as in the form of

$$\mathbf{y} = [\mathbf{y}^{v_1},\ \mathbf{y}^{v_2}, \ldots,\ \mathbf{y}^{v_9}]^T, \tag{18}$$

and

$$\mathbf{y}^{v_j} = \left[I_{\lambda_1}^{v_j}, \ldots,\ I_{\lambda_5}^{v_j},\ Q_{\lambda_2}^{v_j},\ Q_{\lambda_4}^{v_j},\ Q_{\lambda_5}^{v_j},\ U_{\lambda_2}^{v_j},\ U_{\lambda_4}^{v_j},\ U_{\lambda_5}^{v_j} \right]^T, \tag{19}$$

here, the superscript v_j means the multi-viewing angle with $j = 1$, ..., 9.

3.3. Information content analysis model

For information content analysis, we introduce the averaging kernel matrix in the form of

$$\mathbf{A} = \left(\mathbf{K}^T \mathbf{S}_\epsilon^{-1} \mathbf{K} + \mathbf{S}_{\text{a}}^{-1} \right)^{-1} \mathbf{K}^T \mathbf{S}_\epsilon^{-1} \mathbf{K}, \tag{20}$$

where **A** characterizes the changes in the retrieved stated vector $\hat{\mathbf{x}}$ to changes in the true state vector **x**, and the trace of **A** is equivalent to the number of independent pieces of information from the TOA measurements, also called the degree of freedom for signal (DFS) [87–89].

Correspondingly, the DFS of each individual retrieved parameter can be represented by the element $\mathbf{A}_{i,i}$ in the range of 0 and 1, in which the DFS result $\mathbf{A}_{i,i} = 1$ means that the observation is able to fully characterize the truth of x_i; while $\mathbf{A}_{i,i} = 0$ means that the observation do not contain any information on x_i at all. The closer the value of $\mathbf{A}_{i,i}$ to 1, the better the retrieval of parameter x_i; by contrast, the closer the value of $\mathbf{A}_{i,i}$ to 0, the less information content is involved for the retrieval of x_i. As long as the DFS result $\mathbf{A}_{i,i} > 0.5$ in this study, we assume that the retrieval of parameter x_i could be carried out; furthermore, if the DFS result $\mathbf{A}_{i,i} > 0.75$, we assume that the parameter x_i could be regarded as well retrieved.

There are 3 key assumptions should be predefined for applying information content analysis, which includes:

(1) The retrieval was "ideally" designed so that the "best" solution could always be found after several optimized iterations, in which the "best" solution represents the global optimal solution rather than the local optimal solution based on the OE framework [90].
(2) The forward model is perfect, thus the model itself does not have any calculation errors. Besides, the prior errors of retrieval parameters in state vector **x** are mutually independent with each other; the prior errors of predefined parameters in aerosol model vector **b** are also non-correlated [60].
(3) The observational errors, including measurement errors and model errors, are well characterized and conform to Gaussian distribution [66]. The measurement errors are independent among the multi-viewing measurements, while the model errors correspond to propagation of errors in the forward model caused by the prior error of predefined aerosol model [78].

Furthermore, any violation of the above conditions will somehow bias the conclusions in study. Therefore, based on these assumptions, the a priori error covariance matrix $\mathbf{S}_{\text{a}}$ and $\mathbf{S}_{\text{b}}$ can be regarded as a diagonal matrix respectively, and the measurement error covariance matrix $\mathbf{S}_{\text{y}}$ also can be presented in a diagonal form integrated with the 5% radiance calibration errors and 0.02 polarized calibration errors together for DPC instrument. Consequently, the observational covariance matrix $\mathbf{S}_\varepsilon$ could be further obtained by the sum of $\mathbf{S}_{\text{y}}$ and $\mathbf{K}_{\text{b}}\mathbf{S}_{\text{b}}\mathbf{K}_{\text{b}}^T$ in Eq. (20).

4. Test scenarios

4.1. Observation geometry setting

In order to obtain the synthetic data of DPC for information content analysis, 4 multi-viewing observation geometries are considered with the combinations of different solar zenith angles (θ_0), viewing zenith angles (θ_{v}) and relative azimuth angles (ϕ) to represent the typical observations in different location. Here, the summer low and summer high corresponds to the observation with low and high solar zenith angle in summer conditions, respectively, while the winter low and winter high case corresponds to the observation with low and high solar zenith angle in winter conditions respectively, just as listed in Table 2.

Fig. 3(a) plots the polar-plot observational geometries, in which the radius means the θ_{v} change from 0° to 60° with the step of 20°, and the polar angle represents ϕ change from 0° to 360°, as well as the position of Sun also defined with $\phi = 0°$. When $\phi = 0°$, this geometry represents the observer and Sun are in the same direction and also in the same side of main plane, and $\phi = 180°$ corresponds to the opposite direction and side of main plane, so as in other polar-plot figures in this paper. Correspondingly, Fig. 3(b) plots the scattering angles (Θ) based on the observational geometries, with the range of Θ also listed in Table 2.

4.2. Aerosol case setting

To simulate of the synthetic data of DPC measurements, Table 3 lists 4 aerosol model cases, including the fine case, coarse case, polluted and dust cases, just as the results shown in Fig. 4. In which, the fine case ($\text{FMF}_V = 1.0$) and coarse case ($\text{FMF}_V = 0.0$) correspond to the pure fine-mode and coarse-mode aerosols respectively. Based on climatology analyses of Sun-sky radiometer observation network (SONET) measurements [91–94], for the polluted and dust aerosols, we assume that these 2 aerosol cases are mixed with different relative percentage between the fine and coarse modes with the FMF_V equals to 0.5 and 0.2, respectively, which are equivalent to the well-mixed and coarse-dominated aerosols used by other studies [60]. Besides, for test in the optimal estimation scheme, we need to set the a priori errors corresponding to fundamental variables (here the V_0^{f} and V_0^{c}), which are all equal to 80%, respectively in this study.

The detailed values of above particle size distribution and complex refractive index for both fine and coarse mode aerosols are taken from the previous research work [60]. For the fine-mode, the value of $r_{\text{eff}}^{\text{f}}$, $v_{\text{eff}}^{\text{f}}$, m_{r}^{f} and m_{i}^{f} are equal to 0.21, 0.25 μm, 1.44 and 0.011 with the a priori errors of 15%, 15% 0.025 and 50%, respectively; while for the coarse-mode, the value of $r_{\text{eff}}^{\text{c}}$, $v_{\text{eff}}^{\text{c}}$, m_{r}^{c} and m_{i}^{c} are equal to 1.90, 0.41 μm, 1.55 and 0.003 with the a priori error of 35%, 35%, 0.04 and 50%, respectively. Here, the real and imaginary parts are all assumed as independent on the wavelength in this study for simplification, and the a priori error refer to the retrieval errors of Aerosol Robotic Network (AERONET) [95].

Table 2
Multi-viewing observation geometries for forward simulations (corresponding to Fig. 3).

Geometry scenarios	Solar zenith range (°)	Viewing zenith range (°)	Relative azimuth range (°)	Scattering angle range (°)
Case 1 (summer low)	32.80–33.59	25.88–59.78	104.02–248.41	105.05–120.00
Case 2 (summer high)	53.08–53.74	27.96–61.06	88.40–229.85	80.28–109.81
Case 3 (winter low)	54.12–54.19	44.64–64.09	0.60–336.63	111.32–152.18
Case 4 (winter high)	77.63–78.21	32.38–61.87	6.52–334.35	85.48–145.80

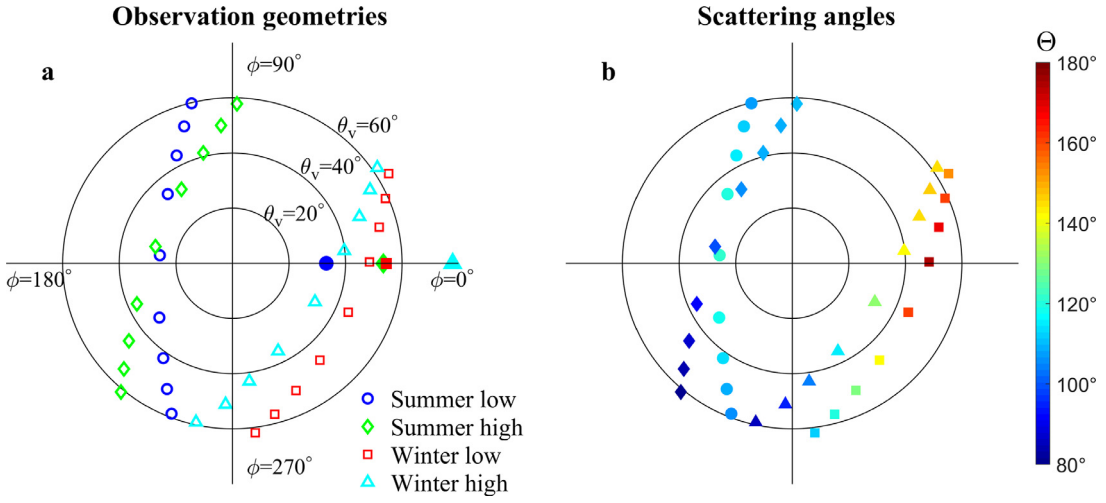

Fig. 3. Multi-viewing observation geometries (a) and corresponding scattering angles (b) for forward simulations and information content analysis. In panel (a), the solid circle, diamond, square and triangle with $\phi = 0°$ represent the corresponding position of the Sun for summer low, summer high, winter low and winter high scenario, respectively.

Table 3
The aerosol scenarios for the synthetic simulations of DPC measurements.

Scenarios	V_0 ($\mu m^3 \mu m^{-2}$)	FMF_V	τ_a (550 nm)	FMF ($\lambda_1 - \lambda_5$)	α
Fine case	0.095	1.0	0.6	1.0	1.51
Coarse case	0.656	0	0.6	0	0.50
Polluted case	0.162	0.5	0.6	0.90, 0.89, 0.88, 0.83, 0.75	1.23
Dust case	0.296	0.2	0.6	0.70, 0.67, 0.62, 0.56, 0.43	0.81

The parameters τ_a represent the total AOD, τ_a (550 nm) represent the total AOD at 550 nm, $\lambda_1 - \lambda_5$ represent the wavelength centered at 443, 490, 565, 670, and 865 nm, respectively, and α represents the Angstrom exponent gained by the AODs at 490 and 865 nm.

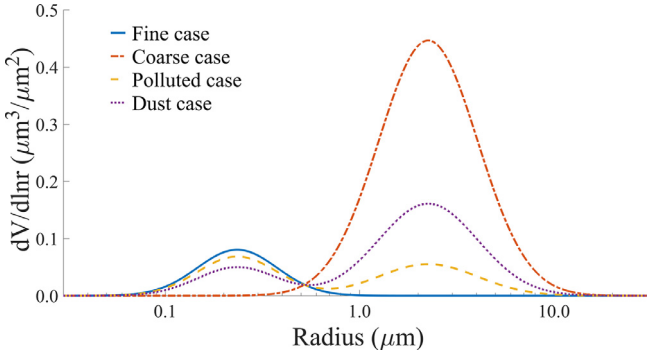

Fig. 4. The volume particle size distributions of the aerosol cases corresponding to Table 3.

It should be noted that these 4 cases are only our "base" cases. In order to comprehensively assess the retrieval capability of DPC, we employ actually a dataset of aerosol cases with varying AOD values from and 0.1 to 2.0 at 550 nm to represent the different aerosol loadings. For example, for τ_a (550 nm) = 0.6, the V_0 can vary from 0.095 to 0.656 $\mu m^3 \mu m^{-2}$ with fmf_V decrease from 1 to 0, respectively for 4 base cases. Correspondingly, aerosol model parameters of other AOD values can be gained with linear scaling.

4.3. Surface model setting

In the forward simulations, we consider two typical surface types, in which the vegetation and bare soil are used to respectively represent the dark surface case (except for the wavelength in 865 nm) and bright surface case. One reason why only choose two surface types is that we are looking for a solid aerosol retrieval in order to test the DPC aerosol retrieval ability once in commissioning, thus we do not need to consider all of the surface types in this study. Besides, the desert surface can be regarded as one of the bare soil surface types for bright surface case [96,97], so we did not consider the desert surface separately in this paper. In addition, previous study has shown that the surface reflectance over land could be estimated by a mixing spectral model of vegetation and bare soil with NDVI [98,99]. Therefore, these two surface types can satisfy the information content analysis for DPC.

Based on the airborne measurements of Research Scanning Polarimeter (RSP) and satellite measurements of POLDER, the parameters of the BRDF and BPDF are chosen from the work of Litvinov et al. [44,100,101], and thus the mixtures of vegetation (e.g. conif-

Table 4
The parameters of the improved BRDF model (this work) and the kernel-driven BRDF models (Ross–Li) for simulations.

Surface type	Band (nm)	Improved BRDF model			Ross–Li BRDF model		
		$f(\lambda)$	k_1	k_2	$f_{iso}(\lambda)$	$k_1(\lambda)$	$k_2(\lambda)$
Vegetation	443	0.0325	0.087	0.668	0.0325	0.0028	0.0217
	490	0.0347			0.0347	0.0030	0.0232
	565	0.0737			0.0737	0.0064	0.0492
	670	0.0395			0.0395	0.0034	0.0264
	865	0.3809			0.3809	0.0331	0.2544
Bare soil	443	0.0705	0.158	0.547	0.0705	0.0111	0.0386
	490	0.1006			0.1006	0.0159	0.0550
	565	0.1720			0.1720	0.0271	0.0940
	670	0.2427			0.2427	0.0383	0.1328
	865	0.3253			0.3253	0.0514	0.1779

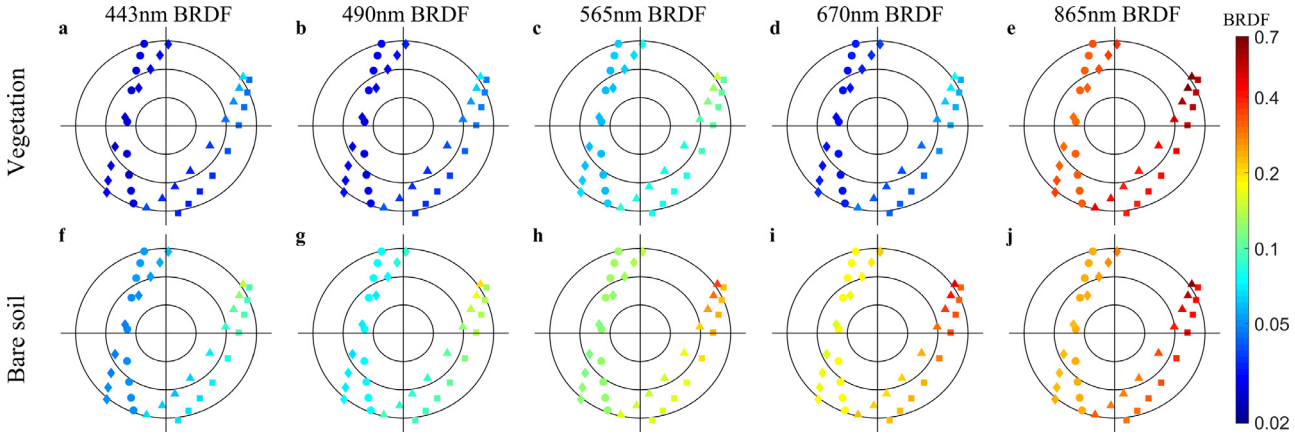

Fig. 5. The angular distribution of BRDF models at DPC bands for vegetation and bare soil surface types, respectively.

Table 5
A priori error of the parameters of BRDF and BPDF models for information content analysis.

Surface type	$f(\lambda)$, $f_{iso}(\lambda)$	$k_1, k_2, k_1(\lambda), k_2(\lambda)$	C
Vegetation	0.0215, 0.0224, 0.0466, 0.0207, 0.2119	80%	40%
Bare soil	0.0425, 0.0495, 0.0777, 0.0917, 0.0792		

erous, savannah, etc.) are also not considered here. Table 4 lists the parameters of the improved BRDF and Ross-Li BRDF models, which satisfy the conditions that $f_{iso}(\lambda)=f(\lambda)$, $k_1(\lambda)=k_1 f(\lambda)$, and $k_2(\lambda)=k_2 f(\lambda)$. Correspondingly, Fig. 5 plots the angular distribution of BRDF at 443, 490, 565, 670 and 865 nm, respectively.

As for the parameters of BPDF models in forward simulations, the NDVI are equal to 0.62 and 0.03, with the parameter C corresponding to 6.57 and 6.90, respectively, for vegetation bare soil surface types [44]. Based on these setting, Fig. 6 illustrates the angular distribution of wavelength-independent BPDF for vegetation and bare soil respectively. From Figs. 5 and 6, we can find that the value difference of BRDF and BPDF mainly depend on the observational geometry and surface type, and the retrieval of wavelength-dependent BRDF parameters will be much more complicated than that of the wavelength-independent BPDF parameter. This is usually thought as one of major advantages of satellite polarimetric remote sensing of aerosols, i.e. simpler surface model helps simplify the surface-atmosphere decoupling, which contributes to extraction of atmospheric information from satellite TOA signals.

In addition, Table 5 lists the a priori errors of the parameters of BRDF model for information content analysis, in which the a priori errors (absolute errors) of $f(\lambda)$ and $f_{iso}(\lambda)$ are equivalent to the standard deviation of surface reflectance datasets from the USGS and ASTER spectral library [97,102], while other parameters such as k_1, k_2, $k_1(\lambda)$ and $k_2(\lambda)$ are all assumed with a priori error of 80% based on the BRDF product of MODIS [103]. Meanwhile, the a priori error of BPDF parameter C is set to 40% based on the work of Maignan et al. [42].

4.4. Synthetic data of DPC measurements

In order to present synthetic data of DPC measurements, we further define the TOA reflectance (R^{TOA}) and polarized reflectance (R_p^{TOA}) as

$$\begin{cases} R^{TOA} = \pi\ I/\mu_0 \\ R_p^{TOA} = \pi\sqrt{Q^2+U^2}/\mu_0 \end{cases}, \tag{21}$$

where the definition of I, Q and U correspond to the Eqs. (2) – (3).

The TOA synthetic data are calculated by UNL-VRTM for a mid-latitude summer/winter atmospheric profile for the summer/winter low and high observation geometries respectively, meanwhile, all of the synthetic data are only cloud free. Fig. 7 illustrates the angular distribution of simulated R^{TOA} at 443, 490, 565, 670 and 865 nm, respectively for the polluted aerosol case with AOD = 0.6. Fig. 8 illustrates the angular distribution of R_p^{TOA}

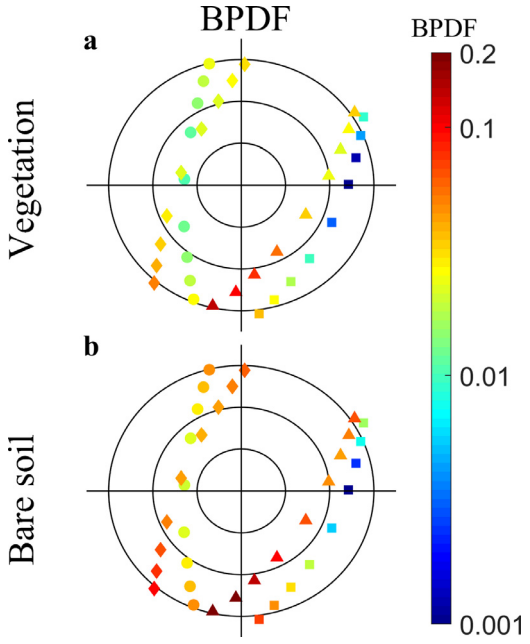

Fig. 6. The angular distribution of wavelength-independent BPDF results for vegetation and bare soil, respectively.

at 3 wavelength bands (443, 490 and 865 nm) with polarimetric measurements for the polluted aerosol case also with AOD = 0.6.

For the R^{TOA} and R_p^{TOA} at the same wavelength, the TOA reflectance for different surface types show obviously difference, to the contrary, TOA polarized reflectance has less difference for different surface types. However, while for the different wavelength, the TOA polarized reflectance also has some varieties along the observational geometries, due to the significant difference of polarized phase functions [79]. For the reason of simplification, TOA measurements corresponding to other 3 aerosol types are not presented in the figure, but the features are similar.

5. Results

5.1. Performance of the improved surface model

In this section, we firstly investigate the information content for the retrieval all the coefficients of the BRDF models, with the assumption that the all of the aerosol properties and BPDF parameter are well characterized. For this purpose, the state vector only contains the BRDF coefficients, i.e. Eq. (16) with all of the aerosol and BPDF parameters removed and with no error propagation of the predefined aerosol model.

Fig. 9 illustrate the DFS of each retrieved parameter of the 2 BRDF models (Ross–Li versus the improved) for the surface type of vegetation and bare soil, respectively, in which the values of DFS and error bar correspond to the mean DFS and standard deviation of 4 multi-viewing observation scenarios. For the traditional (Ross–Li) BRDF model, even though the aerosol and BPDF properties have been fixed, we found that some BRDF parameters are still difficult to be retrieved because of the insufficient information content. For example in the polluted aerosol case, for the vegetation surface type, the DFS of parameters $k_1(\lambda)$ and $k_2(\lambda)$ at bands $\lambda_1-\lambda_4$ are all smaller than 0.5; for the bare soil, the DFS of parameters $k_1(\lambda)$ and $k_2(\lambda)$ at $\lambda_1-\lambda_3$ also cannot exceed 0.5, as well as the DFS value of $f_{iso}(\lambda_5)$. It should be noted that, if the BRDF parameters cannot be well retrieved, then most probably the correct aerosol parameters could also probably not be obtained in the real retrieval. While for the DFS of the improved BRDF model with the same aerosols and surface type cases, all of the 7 parameters including $f(\lambda_1)$, ..., $f(\lambda_5)$, k_1 and k_2 could be well determined, with most of DFS value are larger than 0.75. Therefore, the improved BRDF model with less retrieved parameters is essential in our inversion framework. Then, another vital question arises: can the aerosol and BPDF parameters be retrieved together with these 7 parameters of improved BRDF model? To answer this question, we will give detailed discussion in next subsection.

5.2. Retrieval capability for typical cases

Based on the definition of state vector in Eq. (16) with the use of improved BRDF model, Fig. 10 plot the DFS of the retrieved V_0^f (hence τ_a^f), V_0^c (hence τ_a^c) and surface parameters $f(\lambda_1)$,..., $f(\lambda_5)$, k_1, k_2, C (hence the BRDF and BPDF) together for 4 different aerosol types and 2 surface types respectively. For the single mode aerosols (a–d), the parameter V_0^f could be well retrieved with 8 surface parameters for fine aerosol case, while the parameter V_0^c could also be well retrieved for coarse aerosol case. For the polluted and dust cases, which represents more realistic aerosol characteristics in the atmosphere, both V_0^f and V_0^c also could be well retrieved with the $f(\lambda_1)$,..., $f(\lambda_5)$, k_1, k_2 and C. From Fig. 10, we conclude that:

(1) For the same aerosol type, the retrieval performances are rather constant over different surface types, or well retrieved over various land surfaces. This should thank to the simultaneous re-

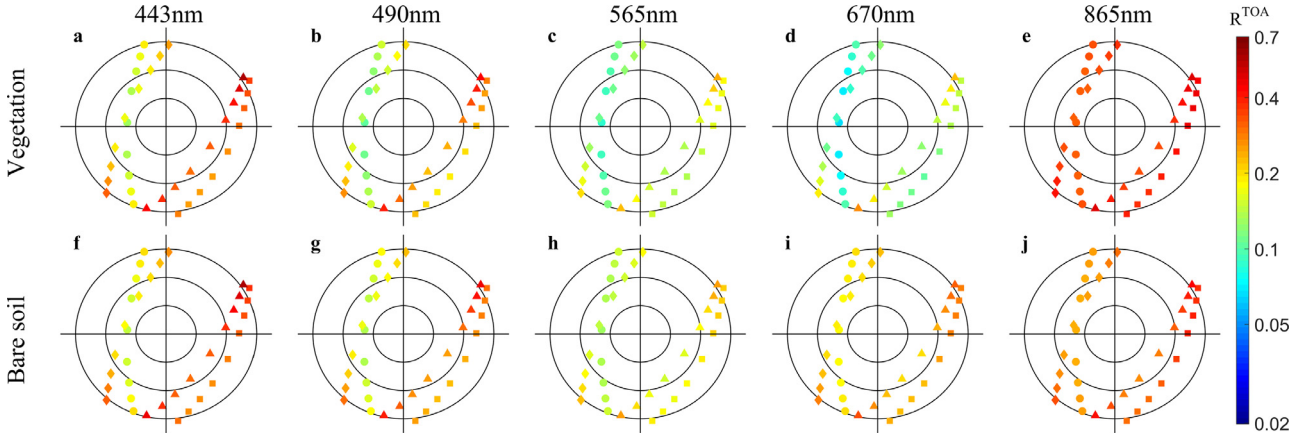

Fig. 7. Simulated TOA reflectance results at each wavelength for polluted case with AOD = 0.6, in which panel (a–e) correspond to the vegetation surface, while (f–j) correspond to the bare soil surface.

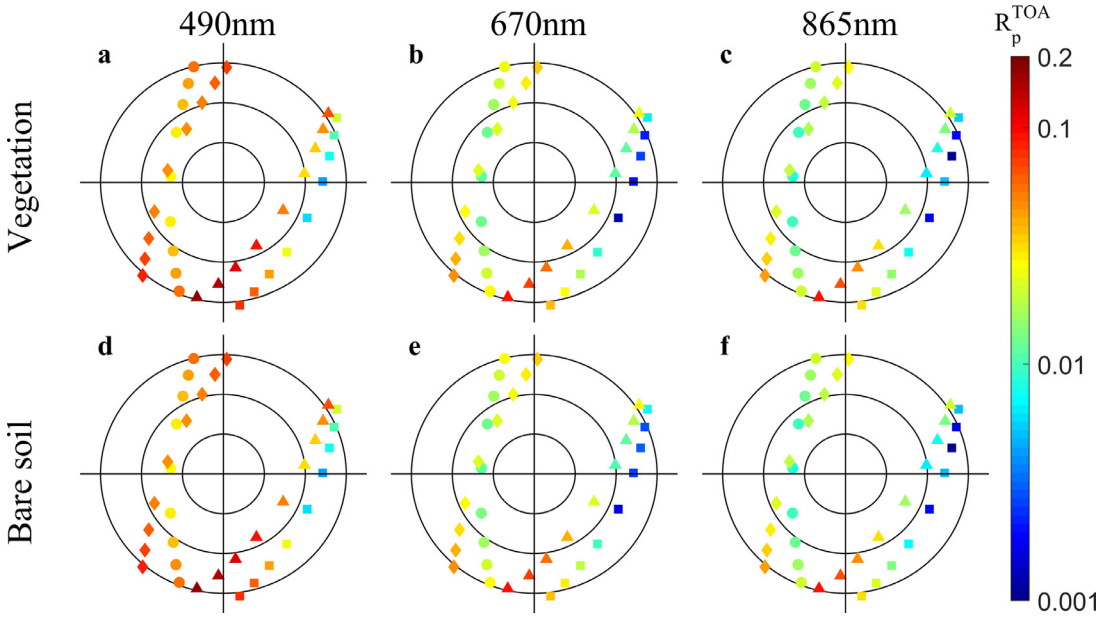

Fig. 8. Simulated TOA polarized reflectance results at 490, 670 and 865 nm for polluted case with AOD = 0.6.

trieval of aerosol and surface parameters (7 for spectral dependent BRDF, 1 for BPDF) together. During the retrieval, the uncertainties attach to surface parameters are slightly larger rather than that of aerosol, especially for the wavelength with smaller surface reflectance (e.g. r_{λ_1} at 443 nm), proved by the different DFS under different surface.

(2) The determination of the coarse mode is relatively difficult rather than the fine mode, e.g., as shown in Fig. 10 (e) and (f). This might be attached to DPC band configuration, which is less of the shortwave infrared (SWIR) wavelength band, e.g. 1.6 or 2.2 μm, which has been proved useful to retrieval coarse particles [82, 104–106]. Moreover, the polarization is also usually thought to less sensitive to coarse particles within the 1.0 μm wavelength bands [35,79,107,108]. Therefore, the wavelength bands centered at 1.6 or 2.2 μm has been integrated in the new-generation spaceborne polarimetric sensors/instruments, such as the Multi-viewing, Multi-channel, Multi-polarisation Imager (3MI) by the European Organization for the Exploitation of Meteorological Satellites (EUMETSAT) [109–111], the Aerosol Polarimetry Sensor (APS) by NASA [112], as well as the Polarization CrossFire (PCF) scheme by China.

(3) For the 2 realistic aerosol types (polluted and dust), the retrieval performances are all quite good in most cases, except that the retrieval of coarse-mode V_0^c in the polluted case over bare soil surface (bright surface) under some geometric conditions may have some difficulties (DFS < 0.5). However, this is expected to be not important in the air pollution monitoring objective of DPC, because during most of anthropogenic polluted conditions, information on fine particles (e.g. $PM_{2.5}$) are much required which can be well retrieved as shown in Fig. 10 (e) and (f).

5.3. Retrieval capability for aerosol spectral optical properties

For the retrieval of aerosol optical parameters, we have considered the retrieval of V_0^f and V_0^c instead of the wavelength-dependent $\tau_a^f(\lambda)$ and $\tau_a^c(\lambda)$ in this study in the previous section. Based on the relationship of Jacobians between $V_0^{f,c}$ and $\tau_a^{f,c}(\lambda)$ [70], however, we can further derivate the relationship by the chain rule for derivative as

$$\begin{cases} \dfrac{\partial \tau_a^f(\lambda)}{\partial V_0^f} = \dfrac{\tau_a^f(\lambda)}{V_0^f} \\ \dfrac{\partial \tau_a^c(\lambda)}{\partial V_0^c} = \dfrac{\tau_a^c(\lambda)}{V_0^c} \end{cases}. \tag{22}$$

So, the information content of V_0^f and V_0^c can be regarded are equivalent to those of spectral $\tau_a^f(\lambda)$ and $\tau_a^c(\lambda)$:

$$Equivalent\ DFS\left[\tau_a^f(\lambda)\right] = DFS\left(V_0^f\right), \tag{23}$$

$$Equivalent\ DFS[\tau_a^c(\lambda)] = DFS(V_0^c). \tag{24}$$

Besides, based on Eq. (5), the equivalent DFS of $\tau_a(\lambda)$ can also be expressed by results of wavelength-independent V_0^f and V_0^c, adjusted by the FMF_V as

$$Equivalent\ DFS[\tau_a(\lambda)\ ] = FMF_V\ DFS\left(V_0^f\right) + (1 - FMF_V)\ DFS(V_0^c), \tag{25}$$

In this way, Table 6 listed the mean equivalent DFS of the retrieved $\tau_a(\lambda)$ for different aerosol models and surface types. The values in the table are average of all geometries and AOD values (τ_a = 0.1 – 2.0 at 550 nm).

For Table 6, we conclude that: (1) over various surface types, the spectral aerosol parameters $\tau_a(\lambda)$ can be well determined (with the lowest DFS of 0.84); while over the vegetation surface, aerosol retrieval performance is better than the bare soil, which agrees with other aerosol retrieval approaches, e.g. Dark target

Table 6
Equivalent DFS of spectral AOD for vegetation and bare soil surface respectively.

Equivalent DFS of $\tau_a(\lambda)$	Vegetation	Bare soil
Fine case	0.99	0.98
Coarse case	0.91	0.88
Polluted case	0.87	0.84
Dust case	0.91	0.89

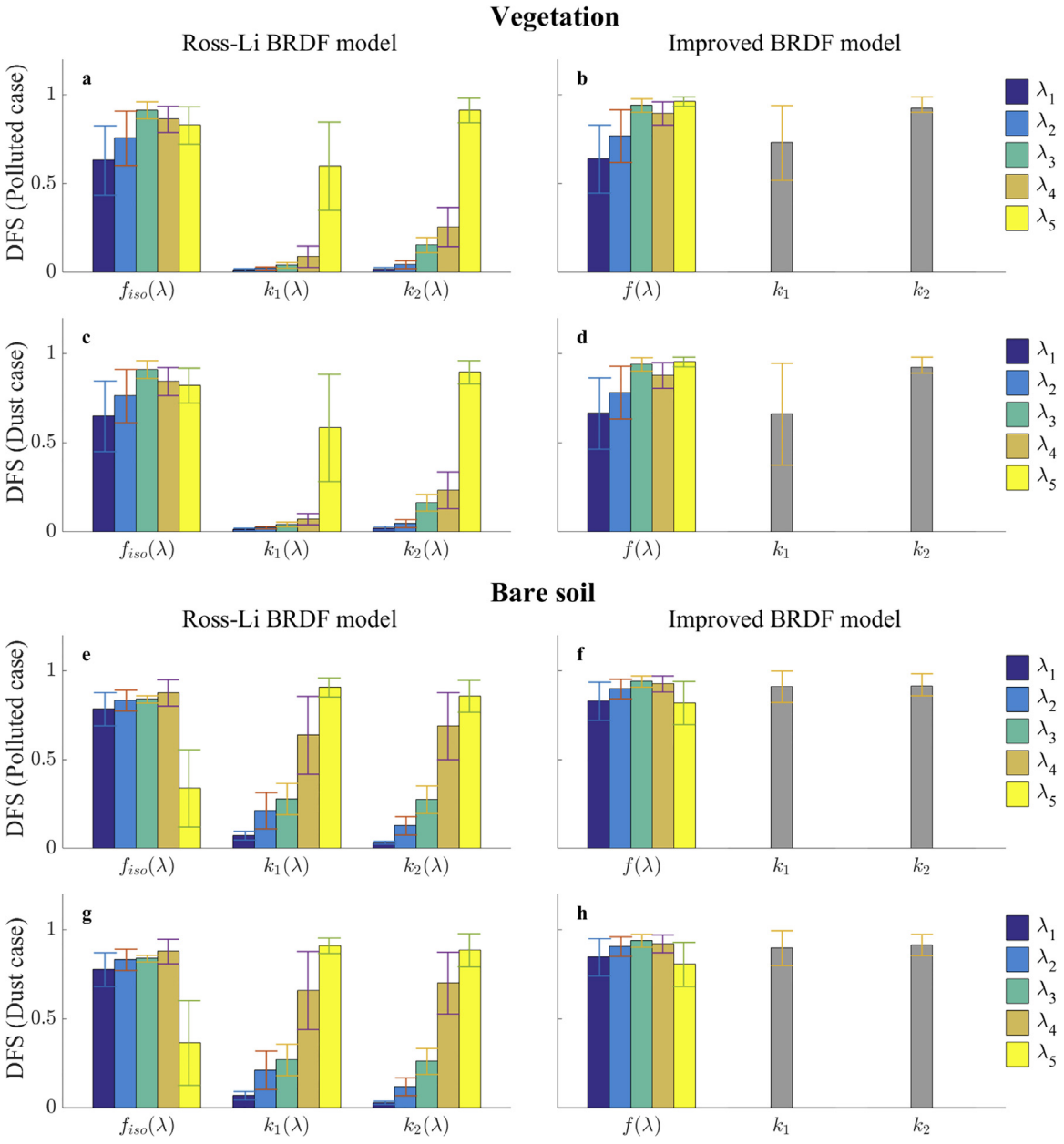

Fig. 9. DFS of each retrieved parameters of the Ross–Li and improved BRDF parameter models. Panel (a–d) and panel (e and f) corresponds to vegetation and bare soil surface type respectively, while the left panel and right panel are for the Ross–Li BRDF and improved BRDF model, respectively.

method [15,18]. (2) For different aerosol types, the retrieval performance varies, in which, the pure fine particles cases can be perfectly determined, and while DFS of the pure coarse particle cases are relatively lower. This explains also the slightly higher DFS in dust case than that of polluted case, because the difficulties in retrieving of lower concentration of coarse particles respect to higher fine particles in the polluted case cumbrance the entire performance for this fairly realistic condition to some extent.

As along as the $\tau_a^f(\lambda)$, $\tau_a^c(\lambda)$ and $\tau_a(\lambda)$ have be analyzed, the Angstrom exponent and fine-mode fraction could be further obtained by Eq. (6)–(7). Because the parameters α and FMF(λ) are calculated from the spectral $\tau_a^f(\lambda)$, $\tau_a^c(\lambda)$ and $\tau_a(\lambda)$, the corresponding error is estimated to inevitably increase, which could be numerically investigated in further study. However, in the content of information content analysis of this work, we believe our results have proved that these optical parameters can be all well obtained from DPC measurements.

6. Discussion

As a “day-1” inversion algorithm for the on-orbit testing, we hope to focus on the major scientific objectives of DPC onboard GF-5 satellite, i.e., the retrieval of AOD and FMF. Here, the so called “day-1” means the first day of operation dissemination, that is, the inversion algorithm should be available immediately after commissioning, similar as the “day-1” product at EUMETSAT [113,114]. However, the inversion framework developed in this paper actually allows the addition of other aerosol parameters such as the particle size distribution and complex refractive index to the state vector. In this section, we mainly discuss the influence of aerosol loading, retrieving other aerosol parameters together and model errors, respectively, on the DFS results of V_0^f and V_0^c (hence spectral AOD and FMF), as well as the DFS of surface properties.

Besides, to easily present the information content of surface parameters together, we define an equivalent DFS of surface parame-

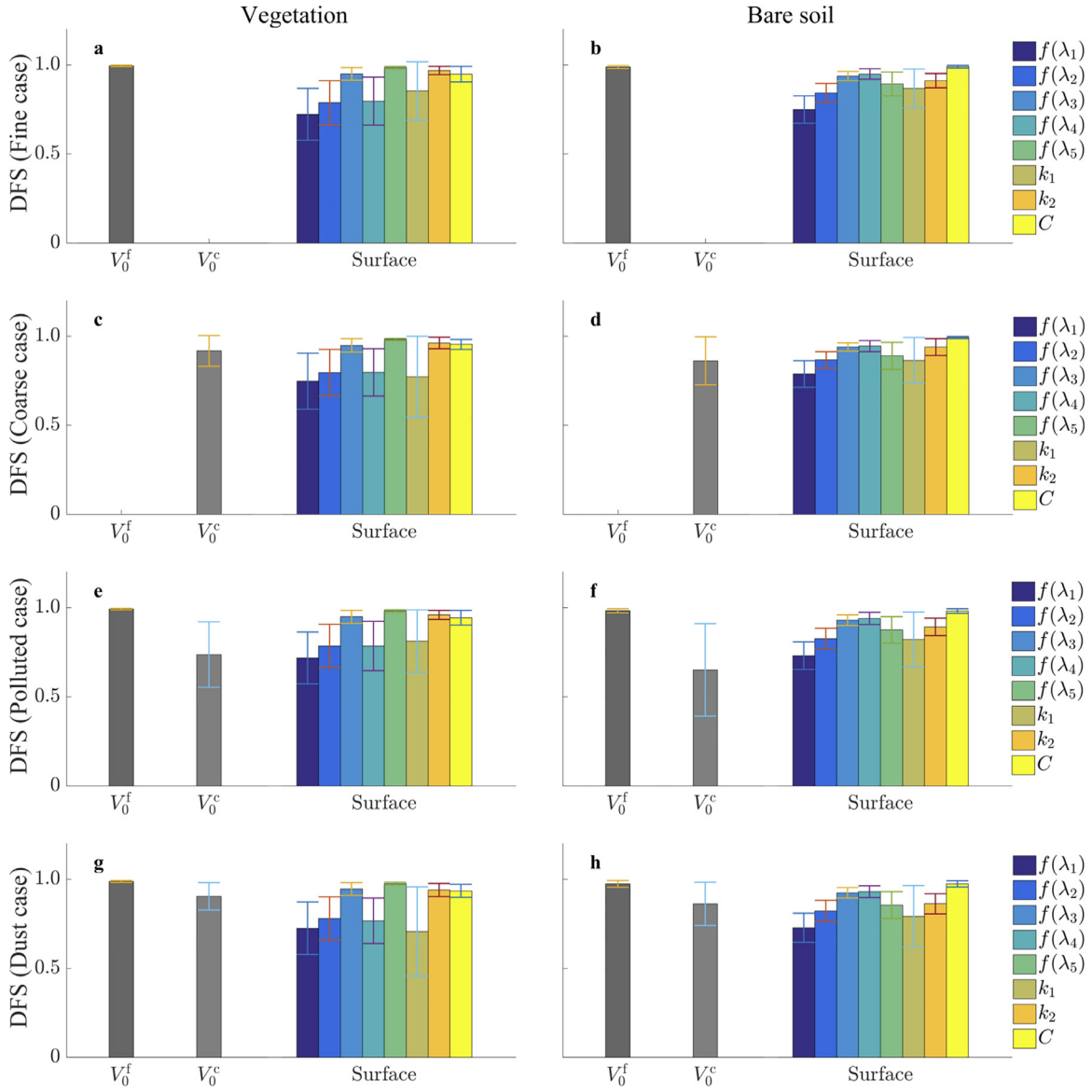

Fig. 10. DFS of the retrieved V_0^f, V_0^c and surface parameters ($f(\lambda_1)$,..., $f(\lambda_5)$, k_1, k_2, C) for different aerosol models with AOD $\tau_a = 0.6$. Panel (a and b), (c and d), (e and f) and (g and h) corresponds to the fine, coarse, polluted and dust case respectively, while the left panel and right panel are for the vegetation and bare soil respectively.

ter S in the form of

$$DFS(S) = \frac{1}{8}\{[DFS[k(\lambda_1)] + \ldots + DFS[k(\lambda_5)] + DFS(k_1) + DFS(k_2) + DFS(C)]\}, \quad (26)$$

where the equivalent DFS of S is equal to the mean DFS of 8 surface parameters. In addation, 2 typical aerosol models including the polluted and dust cases are considered in this section for discussion.

6.1. Influence of aerosol loading variation

Corresponding to Fig. 10, we show in Fig. 11 the DFS of retrieved V_0^f, V_0^c and equivalent surface parameter S as a function of AOD change from 0.1 to 2.0 for vegetation and bare soil surface type respectively. The DFS of aerosol parameters V_0^f and V_0^c increases with the increasing of AOD, and the corresponding information content slightly convergence to saturation. Meanwhile, the equivalent DFS of surface parameter S decreases with the increasing of AOD. For the retrieval of fine-mode parameter V_0^f, all of the DFS results are larger than 0.92 for 2 different aerosols and surface types, even for the small AOD case ($\tau_a = 0.1$), and DFS of the fine-mode V_0^f (hence fine-mode AOD) is noticeable constant after AOD greater than 0.4. For the retrieval of coarse-mode parameter V_0^c, expect for the AOD $\tau_a \leq 0.2$, V_0^c also can be retrieved (i.e. DFS $>$ 0.5) for different scenarios, and the DFS on V_0^c of dust case is obviously larger than polluted case with the difference of 0.2. Besides, for the equivalent surface parameter, S could be also retrieved in most cases with AOD in the range of 0.1 to 2.0. However, when the AOD $\tau_a > 1.5$, the retrieval of equivalent surface parameter S has a larger uncertainty for vegetated surface with the increasing standard deviation.

6.2. Retrieval of additioanl aerosol parameters

In our inversion framework, the retrieved aerosol parameters mainly contain 2 parameters V_0^f and V_0^c, and other aerosol model parameters should be predefined before the retrieval. However, as the aerosol size and complex refractive index has impact on the retrieval uncertainty of V_0^f and V_0^c, the DFS analysis includ-

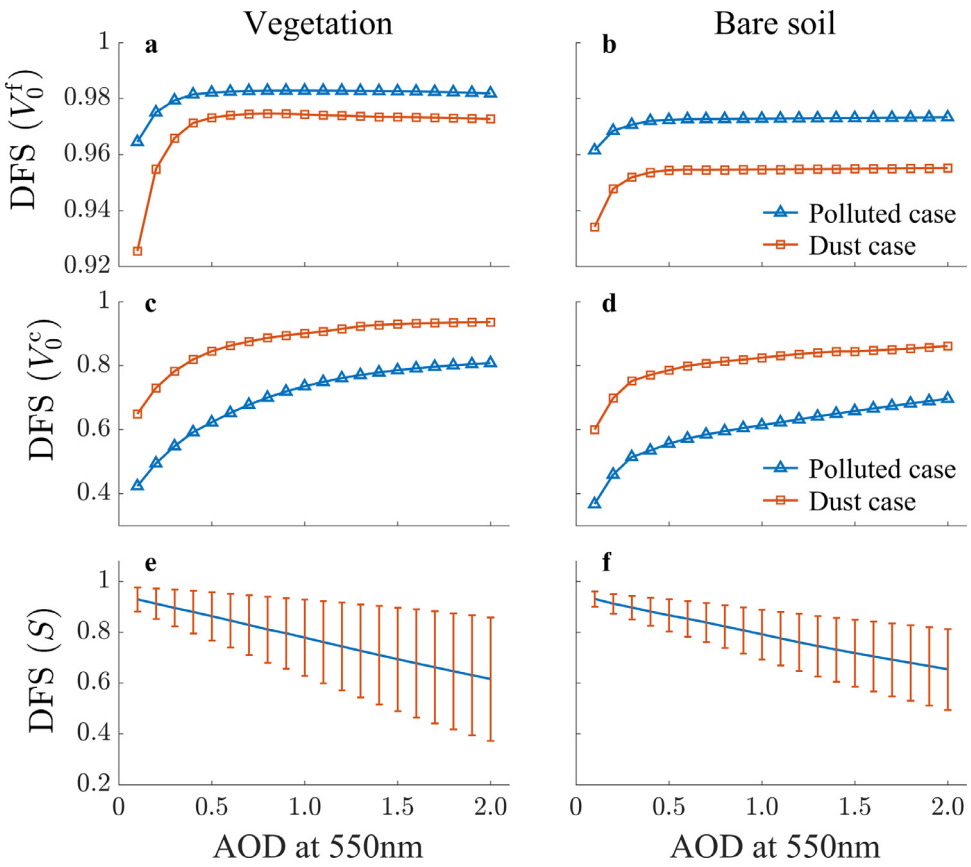

Fig. 11. DFS on the retrieval of V_0^f, V_0^c and equivalent surface parameter S along different AOD from 0.1 to 2.0 at 550 nm, in which left and right panel corresponds to the vegetation and bare soil surface respectively. In panel (e and f), the equivalent DFS and error bar respectively represent the mean DFS and standard deviation calculated from 8 surface parameters including $f(\lambda_1)$,..., $f(\lambda_5)$, k_1, k_2 and C for both polluted and dust cases.

ing these parameters into retrieval state vector is also necessary. Correspondingly, the state vector can be written as

$$\mathbf{x} = \left[V_0^f,\ V_0^c,\ r_{eff}^f,\ v_{eff}^f,\ r_{eff}^c,\ v_{eff}^c,\ m_r^f,\ m_i^f,\ m_r^c,\ m_i^c, f(\lambda_1),\right.$$
$$\left. \ldots,\ f(\lambda_5),\ k_1,\ k_2,\ C\right]^T. \quad (27)$$

In which, we also assume that the real and imaginary parts of complex refractive index are independent of the wavelength in the range of 443 – 865 nm for simplicity. Thus, there are ten aerosol elements need to be retrieved together with the surface parameters. For the DFS calculation, by following our previous work [79], the prior errors of r_{eff}^f, v_{eff}^f, r_{eff}^c, v_{eff}^c are all set to 80%, the prior errors of m_r^f and m_r^c are equal to 0.15, and the prior errors of m_i^f and m_i^c are 0.01 and 0.005, respectively.

Fig. 12 illustrates the DFS component of the retrieved aerosol parameter in Eq. (27) for 2 mixed aerosol types and 2 surface types, respectively. For one thing, not all of the aerosol microphysical parameters could be retrieved simultaneously due to the limited information content of DPC. For example, the aerosol parameters V_0^c, m_i^c, v_{eff}^f, r_{eff}^c and v_{eff}^c cannot be universally retrieved for polluted case, while the parameters m_i^f, v_{eff}^f and v_{eff}^c also cannot be retrieved for dust case. For another, as detailedly listed in Table 7, the DFS results of V_0^f and V_0^c have a certain degree of decrease when the parameters of aerosol size and refractive index are added into the retrieval state vector. In particular, the DFS of V_0^c decreases significantly by 0.1–0.2, and then the V_0^c cannot be retrieved in some case owning to the insufficient information content.

In addition, the scientific objective of DPC is to retrieve spectral AOD $\tau_a(\lambda)$, instead of determining simultaneously all detailed aerosol microphysical parameters (e.g. effective radius and refractive index) together. This objective result mainly from compromise of various application purposes with a moderate consideration of DPC capability. Thus, the key parameters such as V_0^f and V_0^c should be preferentially selected for retrieval in the inversion framework. Furthermore, this inversion framework can be easily extended for the retrieval of more aerosol parameters, and we will straightforwardly to test the supplement of jointly retrieved aerosol parameters step by step in the next study. Therefore, we exclude the parameters of aerosol size and complex refractive index from being directing retrieved, and further allocate their influence into the aerosol model errors in the paper.

Table 7
Comparison of DFS results of V_0^f and V_0^c (AOD $\tau_a = 0.6$) between excluding the aerosol model parameters in Eq. (16) and including the aerosol model parameters in Eq. (27).

Scenarios	DFS	State vector in Eq. (16)		State vector in Eq. (27)	
		V_0^f	V_0^c	V_0^f	V_0^c
Vegetation	Polluted case	0.992	0.738	0.986	0.569
	Dust case	0.988	0.905	0.978	0.816
Bare soil	Polluted case	0.982	0.652	0.964	0.487
	Dust cast	0.974	0.863	0.943	0.753

6.3. Influence of model errors

Since the predefined aerosol models will inevitably bring some model errors to the retrieval of key aerosol and surface parameters in the inversion framework, then we also need to investigate the influences of predefined model errors on the retrieval results of aerosol and surface parameters quantitatively. Based on the def-

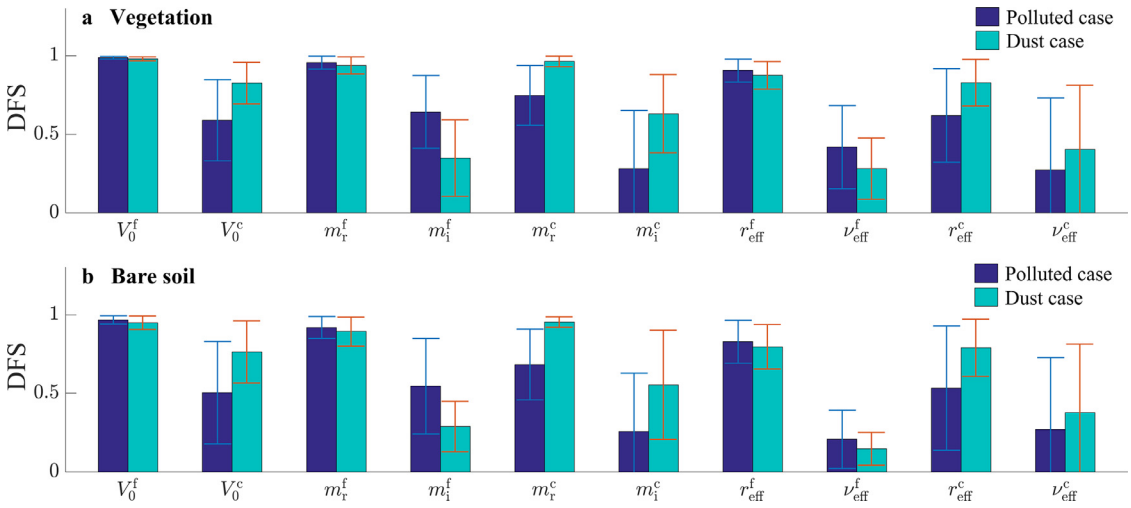

Fig. 12. Same as Fig. 10 with AOD $\tau_a = 0.6$, but for the DFS component of each retrieved aerosol parameter in Eq. (27), and the DFS results of surface parameters are not shown.

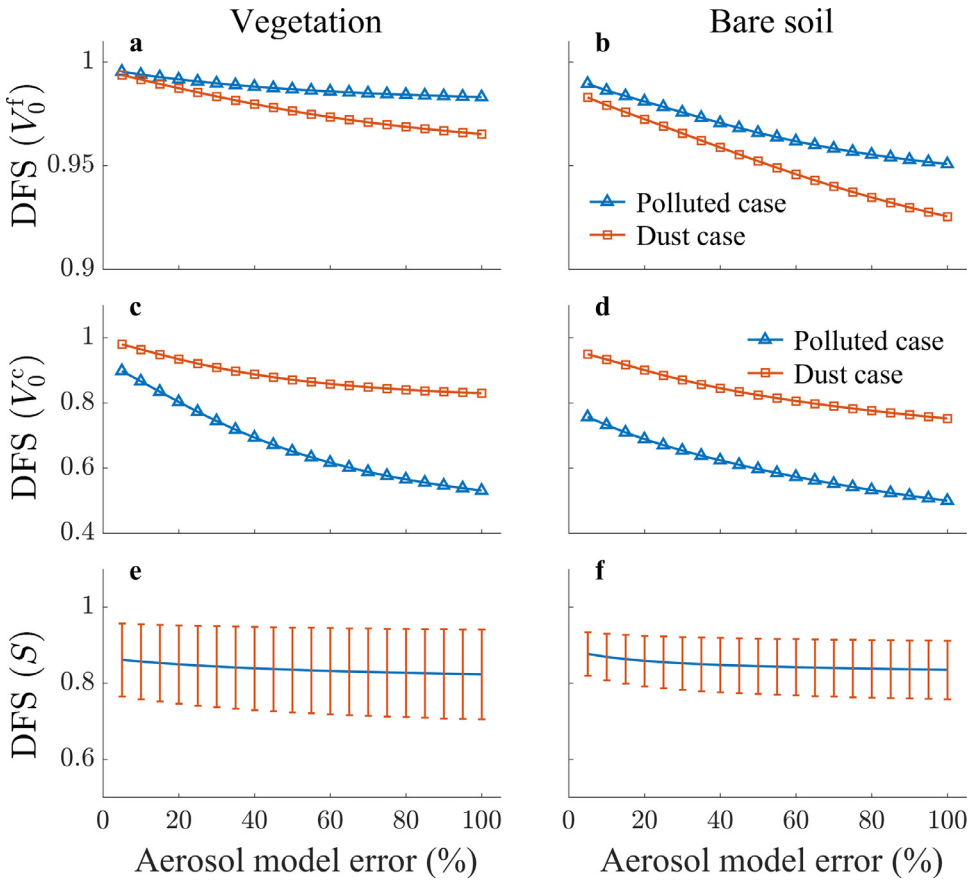

Fig. 13. Same as Fig. 11 but for as a function of the aerosol model errors from 5% to 100% by a step of 5% with AOD = 0.6.

inition of aerosol model parameters in Eq. (17), we analyze the DFS results originating from different model errors with the predefined constant measurement errors as previous section. As a demonstration, we focus on the AOD = 0.6 case for the polluted and dust cases, respectively.

Fig. 13 shows the DFS of retrieved V_0^f, V_0^c and equivalent surface parameter S as a function of the aerosol model errors. Here, the aerosol model errors correspond with the combination of 6 predefined aerosol parameters $\{r_{eff}^f,\ v_{eff}^f, r_{eff}^c,\ v_{eff}^c, m_i^f,\ m_i^c\}$, which are all assumed to change from 5% to 100% by a step of 5% with the constant measurement error, as well as the constant a priori errors of m_r^f and m_r^c which have been defined in Section 4.2. Here, we did not consider the error disturbance for the real part of complex refractive index, because the values range of m_r^f and m_r^c are usually about 1.33–1.60 [115], and a priori errors cannot exceed 20% in the measurement from AERONET [116]. Thus, to maintain the consistency in model error varying from 5% to 100%, we assume that the a priori errors of m_r^f and m_r^c are not change in this assesment.

As shown in the figure, the DFS of each retrieved parameter decreases with the increasing of the aerosol model errors. How-

ever, it is striking to see that even though the aerosol model error reaches 100%, the parameters V_0^f, V_0^c and S still could be retrieved (i.e. DFS > 0.5). In addition, by choosing the aerosol models combined by the fine-mode and coarse-mode parts in the inversion scheme, we find that the aerosol model error has a relative smaller effect on the retrieval uncertainties, especially for the fine-mode V_0^f and equivalent surface parameter S. Moreover, in the actual retrieval of DPC measurements, an iteration procedure among several predefined typical aerosol models has been designed to further decrease the probability to choose a very bad (e.g. model error exceeds 100%) predefined aerosol model.

7. Conclusions

The directional polarized camera (DPC) is a 3.3 × 3.3 km resolution multi-angle polarized imager with wide swath (1850 km) and quick revisiting capability (2 days) on board the Chinese GF-5 satellite. In order to assess its aerosol retrieval performance, we developed an inversion scheme based on optimal estimation theory by utilizing fruitful observation information of DPC (at least 99 measurements for per pixel), to simultaneously determine aerosol spectral optical parameters over land surfaces. The improved BRDF and BPDF models are jointly used in a vector radiative transfer model to construct a compact forward model. By employing the information content analysis approach based on the degree of freedom for signal (DFS), we performed a comprehensive assessment on the DPC aerosol parameter retrieval performance, with setting various aerosol types (4 types), loading (AOD from 0.1 to 2), changing surface types (vegetation, bare soil) and wide range of observation geometries (summer and winter with low and high sun zenith, respectively). The results suggest that:

(1) The spectral AOD can be well retrieved over land surface with fine and coarse mode proportions, which provides also a basis to obtain Angstrom exponent and fine-mode fraction parameters.
(2) The aerosol retrieval performance is quite good over various surface types, based on the uses of improved BRDF and BPDF models as well as the retrieval strategy.
(3) The determination of coarse mode is relatively difficult than fine mode, which suggests a requirement for supplementing SWIR channel on the current DPC band configuration, especially for the wavelength bands centered at 1.6 or 2.2 μm employed in 3MI, APS and PCF.
(4) The aerosol retrieval performance is still better over vegetation than over bare soil surface, which is similar with previous dark target method.

Acknowledgment

This study was support by National Key R&D Program of China [grant number 2016YFE0201400], the National Natural Science Foundation of China [grant numbers 41671367, 41505022], and the Open Fund of State Key Laboratory of Remote Sensing Science [grant number OFSLRSS201710]. Jun Wang is supported by the CCAD start-up funds for the faculty in the University of Iowa. We also acknowledge Shanghai Academy of Spaceflight Technology (SAST) for providing the prototype structure figure of GF-5 satellite.

Supplementary materials

Supplementary material associated with this article can be found, in the online version, at doi:10.1016/j.jqsrt.2018.07.003.

Reference

[1] IPCC. Climate change 2014: synthesis report. Geneva, Switzerland: IPCC; 2014.
[2] Xie Y, Li Z, Zhang Y, Zhang Y, Li D, Li K, et al. Estimation of atmospheric aerosol composition from ground-based remote sensing measurements of Sun-sky radiometer. J Geophys Res Atmos 2017;122:498–518.
[3] Mishchenko MI, Cairns B, Hansen JE, Travis LD, Burg R, Kaufman YJ, et al. Monitoring of aerosol forcing of climate from space: analysis of measurement requirements. J Quant Spectrosc Radiat 2004;88:149–61.
[4] Zhang Y, Li Z. Remote sensing of atmospheric fine particulate matter (PM2.5) mass concentration near the ground from satellite observation. Remote Sens Environ 2015;160:252–62.
[5] Li Z, Zhang Y, Shao J, Li B, Hong J, Liu D, et al. Remote sensing of atmospheric particulate mass of dry PM2.5 near the ground: method validation using ground-based measurements. Remote Sens Environ 2016;173:59–68.
[6] WHO Regional Office for Europe, OECD. Economic cost of the health impact of air pollution in Europe: clean air, health and wealth. Copenhagen: WHO Regional Office for Europe; 2015.
[7] WHO. Health and the environment: addressing the health impact of air pollution. The Sixty-eighth World Health Assembly, WHO; 2015.
[8] Kaufman YJ, Tanre D, Boucher O. A satellite view of aerosols in the climate system. Nature 2002;419:215–23.
[9] Mishchenko MI, Geogdzhayev IV, Cairns B, Carlson BE, Chowdhary J, Lacis AA, et al. Past, present, and future of global aerosol climatologies derived from satellite observations: a perspective. J Quant Spectrosc Radiat 2007;106:325–47.
[10] Mishchenko MI, Liu L, Geogdzhayev IV, Li J, Carlson BE, Lacis AA, et al. Aerosol retrievals from channel-1 and -2 AVHRR radiances: long-term trends updated and revisited. J Quant Spectrosc Radiat 2012;113:1974–80.
[11] Mishchenko MI, Travis LD. Satellite retrieval of aerosol properties over the ocean using polarization as well as intensity of reflected sunlight. J Geophys Res 1997;102:16989.
[12] Kahn R, Banerjee P, McDonald D, Diner D. Sensitivity of multiangle imaging to aerosol optical depth and to pure-particle size distribution and composition over ocean. J Geophys Res 1998:103.
[13] Mishchenko MI, Travis LD. Satellite retrieval of aerosol properties over the ocean using measurements of reflected sunlight: Effect of instrumental errors and aerosol absorption. J Geophys Res Atmos 1997;102:13543–53.
[14] Kaufman YJ, Wald AE, Remer LA, Gao B-C, Li R-R, Flynn L. The MODIS 2.1-μm channel—correlation with visible reflectance for use in remote sensing of aerosol. IEEE T Geosci Remote 1997;35:1286–98.
[15] Kaufman YJ, Tanré D, Remer LA, Vermote EF, Chu A, Holben BN. Operational remote sensing of tropospheric aerosol over land from EOS moderate resolution imaging spectroradiometer. J Geophys Res 1997;102:17051–67.
[16] Remer LA, Kaufman YJ, Tanré D, Mattoo S, Chu DA, Martins JV, et al. The MODIS aerosol algorithm, products, and validation. J Atmos Sci 2005;62:947–73.
[17] Levy RC, Remer LA, Mattoo S, Vermote EF, Kaufman YJ. Second-generation operational algorithm: retrieval of aerosol properties over land from inversion of Moderate Resolution Imaging Spectroradiometer spectral reflectance. J Geophys Res Atmos 2007;112.
[18] Levy RC, Remer LA, Kleidman RG, Mattoo S, Ichoku C, Kahn R, et al. Global evaluation of the collection 5 MODIS dark-target aerosol products over land. Atmos Chem Phys 2010;10:10399–420.
[19] Levy RC, Mattoo S, Munchak LA, Remer LA, Sayer AM, Patadia F, et al. The collection 6 MODIS aerosol products over land and ocean. Atmos Meas Tech 2013;6:2989–3034.
[20] Hsu NC, Si-Chee T, King MD, Herman JR. Deep blue retrievals of Asian aerosol properties during ACE-Asia. IEEE Trans Geosci Remote Sens 2006;44:3180–95.
[21] Hsu NC, Jeong MJ, Bettenhausen C, Sayer AM, Hansell R, Seftor CS, et al. Enhanced deep blue aerosol retrieval algorithm: the second generation. J Geophys Res Atmos 2013;118:9296–315.
[22] North PRJ. Estimation of aerosol opacity and land surface bidirectional reflectance from ATSR-2 dual-angle imagery: operational method and validation. J Geophys Res Atmos 2002;107 AAC 4-1–AAC 4-10.
[23] Kokhanovsky AA, Curier RL, De Leeuw G, Grey WMF, Lee KH, Bennouna Y, et al. The inter-comparison of AATSR dual-view aerosol optical thickness retrievals with results from various algorithms and instruments. Int J Remote Sens 2009;30:4525–37.
[24] Sundström AM, Kolmonen P, Sogacheva L, de Leeuw G. Aerosol retrievals over China with the AATSR dual view algorithm. Remote Sens Environ 2012;116:189–98.
[25] de Leeuw G, Holzer-Popp T, Bevan S, Davies WH, Descloitres J, Grainger RG, et al. Evaluation of seven European aerosol optical depth retrieval algorithms for climate analysis. Remote Sens Environ 2015;162:295–315.
[26] Diner DJ, Martonchik JV, Kahn RA, Pinty B, Gobron N, Nelson DL, et al. Using angular and spectral shape similarity constraints to improve MISR aerosol and surface retrievals over land. Remote Sens Environ 2005;94:155–71.
[27] Martonchik JV, Kahn RA, Diner DJ. Retrieval of aerosol properties over land using MISR observations. In: Kokhanovsky AA, de Leeuw G, editors. Satellite aerosol remote sensing over land. Chichester, UK: Springer; 2009. p. 267–92.
[28] Kahn RA, Gaitley BJ, Garay MJ, Diner DJ, Eck TF, Smirnov A, et al. Multiangle Imaging SpectroRadiometer global aerosol product assessment by comparison with the aerosol robotic network. J Geophys Res Atmos 2010;115:D23209.
[29] Kokhanovsky AA, Breon FM, Cacciari A, Carboni E, Diner D, Di Nicolantonio W, et al. Aerosol remote sensing over land: a comparison of satellite retrievals using different algorithms and instruments. Atmos Res 2007;85:372–94.
[30] Herman M, Deuzé JL, Devaux C, Goloub P, Bréon FM, Tanré D. Remote sens-

ing of aerosols over land surfaces including polarization measurements and application to POLDER measurements. J Geophys Res 1997;102:17039.
[31] Li Z, Goloub P, Dubovik O, Blarel L, Zhang W, Podvin T, et al. Improvements for ground-based remote sensing of atmospheric aerosol properties by additional polarimetric measurements. J Quant Spectrosc Radiat 2009;110:1954–61.
[32] Kokhanovsky AA, Davis AB, Cairns B, Dubovik O, Hasekamp OP, Sano I, et al. Space-based remote sensing of atmospheric aerosols: the multi-angle spectro-polarimetric frontier. Earth-sci Rev 2015;145:85–116.
[33] Deschamps PY, Breon FM, Leroy M, Podaire A, Bricaud A, Buriez JC, et al. The POLDER mission: instrument characteristics and scientific objectives. IEEE Trans Geosci Remote Sens 1994;32:598–615.
[34] Herman M, Deuze J-L, Marchand A, Roger B, Lallart P. Aerosol remote sensing from POLDER/ADEOS over the ocean: improved retrieval using a nonspherical particle model. J Geophys Res 2005;110:D10S02.
[35] Deuzé JL, Bréon FM, Devaux C, Goloub P, Herman M, Lafrance B, et al. Remote sensing of aerosols over land surfaces from POLDER-ADEOS-1 polarized measurements. J Geophys Res 2001;106:4913–26.
[36] Tanré D, Bréon FM, Deuzé JL, Dubovik O, Ducos F, François P, et al. Remote sensing of aerosols by using polarized, directional and spectral measurements within the A-Train: the PARASOL mission. Atmos Meas Tech 2011;4:1383–95.
[37] Deuzé JL, Goloub P, Herman M, Marchand A, Perry G, Susana S, et al. Estimate of the aerosol properties over the ocean with POLDER. J Geophys Res 2000;105:15329.
[38] Costantino L, Bréon F-M. Analysis of aerosol-cloud interaction from multi--sensor satellite observations. Geophys Res Lett 2010;37 n/a-n/a.
[39] Dubovik O, Herman M, Holdak A, Lapyonok T, Tanré D, Deuzé JL, et al. Statistically optimized inversion algorithm for enhanced retrieval of aerosol properties from spectral multi-angle polarimetric satellite observations. Atmos Meas Tech 2011;4:975–1018.
[40] Dubovik O, Lapyonok T, Litvinov P, Herman M, Fuertes D, Ducos F, et al. GRASP: a versatile algorithm for characterizing the atmosphere. SPIE Newsroom 2014.
[41] Nadal F, Breon FM. Parameterization of surface polarized reflectance derived from POLDER spaceborne measurements. IEEE T Geosci Remote 1999;37:1709–18.
[42] Maignan F, Bréon F-M, Fédèle E, Bouvier M. Polarized reflectances of natural surfaces: Spaceborne measurements and analytical modeling. Remote Sens Environ 2009;113:2642–50.
[43] Waquet F, Léon J-F, Cairns B, Goloub P, Deuzé J-L, Auriol F. Analysis of the spectral and angular response of the vegetated surface polarization for the purpose of aerosol remote sensing over land. Appl Opt 2009;48:1228–36.
[44] Litvinov P, Hasekamp O, Cairns B. Models for surface reflection of radiance and polarized radiance: comparison with airborne multi-angle photopolarimetric measurements and implications for modeling top-of-atmosphere measurements. Remote Sens Environ 2011;115:781–92.
[45] Gu X, Tong X. Overview of China earth observation satellite programs. IEEE Geosci Remote Sens Mag 2015;3:113–29.
[46] Chen X, Xing J, Liu L, Li Z, Mei X, Fu Q, et al. In-Flight Calibration of GF-1/WFV visible channels using Rayleigh scattering. Remote Sens 2017;9:513.
[47] Tian B, Li Z, Zhang M, Huang L, Qiu Y, Li Z, et al. Mapping Thermokarst lakes on the Qinghai–Tibet plateau using nonlocal active contours in Chinese GaoFen-2 multispectral imagery. IEEE J Sel Topics Appl Earth Obs Remote Sens 2017;10:1687–700.
[48] Sun J, Yu W, Deng Y. The SAR payload design and performance for the GF-3 Mission. Sensors 2017;17:2419.
[49] Yang A, Zhong B, Wu S, Liu Q. Radiometric cross-calibration of GF-4 in multispectral bands. Remote Sens 2017;9:232.
[50] Ye X, Ren H, Liu R, Qin Q, Liu Y, Dong J. Land surface temperature estimate from Chinese Gaofen-5 satellite data using split-window algorithm. IEEE Trans Geosci Remote Sens 2017;55:5877–88.
[51] Ren H, Ye X, Liu R, Dong J, Qin Q. Improving land surface temperature and emissivity retrieval from the Chinese Gaofen-5 satellite using a hybrid algorithm. IEEE Trans Geosci Remote Sens 2018;56:1080–90.
[52] Zhang C, Liu C, Wang Y, Si F, Zhou H, Zhao M, et al. Preflight evaluation of the performance of the Chinese environmental trace gas monitoring instrument (EMI) by spectral analyses of nitrogen dioxide. IEEE Trans Geosci Remote Sens 2018;56:3323–32.
[53] Liu Y, Yang D. Advancements in theory of GHG observation from space. Sci Bull 2016;61:349–52.
[54] Cheng TH, Gu XF, Xie DH, Li ZQ, Yu T, Chen XF. Simultaneous retrieval of aerosol optical properties over the Pearl River Delta, China using multi--angular, multi-spectral, and polarized measurements. Remote Sens Environ 2011;115:1643–52.
[55] Gu X, Cheng T, Xie D, Li Z, Yu T, Chen H. Analysis of surface and aerosol polarized reflectance for aerosol retrievals from polarized remote sensing in PRD urban region. Atmos Environ 2011;45:6607–12.
[56] Chen X, Wang J, Liu Y, Xu X, Cai Z, Yang D, et al. Angular dependence of aerosol information content in CAPI/TanSat observation over land: effect of polarization and synergy with A-train satellites. Remote Sens Environ 2017;196:163–77.
[57] Hagolle O, Goloub P, Deschamps P-Y, Cosnefroy H, Briottet X, Bailleul T, et al. Results of POLDER in-flight calibration. IEEE Trans Geosci Remote Sens 1999;37:1550–66.
[58] Goloub P, Waquet F, Deuze JL, Herman M, Auriol F, Leon JF, et al. Development of a multispectral polarimeter dedicated to aerosol characterization - preliminary results. In: Proceedings of the 2003 IEEE international geoscience and remote sensing symposium proceedings (IEEE Cat No03CH37477); 2003. p. 2164–6.
[59] Bréon F-M. Parasol level-1 product data format and user manual. Paris: the Centre National d'Etudes Spatiales (CNES); 2006.
[60] Xu X, Wang J. Retrieval of aerosol microphysical properties from AERONET photopolarimetric measurements: 1. Information content analysis. J Geophys Res Atmos 2015;120:7059–78.
[61] Xu X, Wang J, Zeng J, Spurr R, Liu X, Dubovik O, et al. Retrieval of aerosol microphysical properties from AERONET photopolarimetric measurements: 2. A new research algorithm and case demonstration. J Geophys Res Atmos 2015;120:7079–98.
[62] Xu X, Wang J, Henze DK, Qu W, Kopacz M. Constraints on aerosol sources using GEOS-Chem adjoint and MODIS radiances, and evaluation with multisensor (OMI, MISR) data. J Geophys Res Atmos 2013;118:6396–413.
[63] Schuster GL, Dubovik O, Holben BN. Angstrom exponent and bimodal aerosol size distributions. J Geophys Res 2006;111.
[64] Yu H, Chin M, Remer LA, Kleidman RG, Bellouin N, Bian H, et al. Variability of marine aerosol fine-mode fraction and estimates of anthropogenic aerosol component over cloud-free oceans from the Moderate Resolution Imaging Spectroradiometer (MODIS). J Geophys Res Atmos 2009;114.
[65] Zhang Y, Li Z, Qie L, Zhang Y, Liu Z, Chen X, et al. Retrieval of aerosol fine–mode fraction from intensity and polarization measurements by PARASOL over East Asia. Remote Sens 2016;8:417.
[66] Waquet F, Cairns B, Knobelspiesse K, Chowdhary J, Travis LD, Schmid B, et al. Polarimetric remote sensing of aerosols over land. J Geophys Res 2009;114:D01206.
[67] Roujean J-L, Leroy M, Deschamps P-Y. A bidirectional reflectance model of the Earth's surface for the correction of remote sensing data. J Geophys Res Atmos 1992;97:20455–68.
[68] Li X, Strahler AH. Geometric-optical bidirectional reflectance modeling of the discrete crown vegetation canopy: effect of crown shape and mutual shadowing. IEEE Trans Geosci Remote Sens 1992;30:276–92.
[69] Wanner W, Li X, Strahler AH. On the derivation of kernels for kernel-driven models of bidirectional reflectance. J Geophys Res Atmos 1995;100:21077–89.
[70] Wang J, Xu X, Ding S, Zeng J, Spurr R, Liu X, et al. A numerical testbed for remote sensing of aerosols, and its demonstration for evaluating retrieval synergy from a geostationary satellite constellation of GEO-CAPE and GOES-R. J Quant Spectrosc Radiat 2014;146:510–28.
[71] Spurr R. VLIDORT: a linearized pseudo-spherical vector discrete ordinate radiative transfer code for forward model and retrieval studies in multilayer multiple scattering media. J Quant Spectrosc Radiat 2006;102:316–42.
[72] Spurr R, Wang J, Zeng J, Mishchenko MI. Linearized T-matrix and Mie scattering computations. J Quant Spectrosc Radiat 2012;113:425–39.
[73] Spurr R. A new approach to the retrieval of surface properties from earthshine measurements. J Quant Spectrosc Radiat 2004;83:15–46.
[74] Zhang Q, Quan J, Tie X, Li X, Liu Q, Gao Y, et al. Effects of meteorology and secondary particle formation on visibility during heavy haze events in Beijing, China. Sci Total Environ 2015;502:578–84.
[75] Xu X, Wang J, Wang Y, Zeng J, Torres O, Yang Y, et al. Passive remote sensing of altitude and optical depth of dust plumes using the oxygen A and B bands: first results from EPIC/DSCOVR at Lagrange-1 point. Geophys Res Lett 2017;44:7544–54.
[76] Xu X, Wang J, Wang Y, Henze DK, Zhang L, Grell GA, et al. Sense size-dependent dust loading and emission from space using reflected solar and infrared spectral measurements: an observation system simulation experiment. J Geophys Res Atmos 2017;122:8233–54.
[77] Hou W, Wang J, Xu X, Reid JS, Han D. An algorithm for hyperspectral remote sensing of aerosols: 1. Development of theoretical framework. J Quant Spectrosc Radiat 2016;178:400–15.
[78] Hou W, Wang J, Xu X, Reid JS. An algorithm for hyperspectral remote sensing of aerosols: 2. Information content analysis for aerosol parameters and principal components of surface spectra. J Quant Spectrosc Radiat 2017;192:14–29.
[79] Hou W, Li Z, Wang J, Xu X, Goloub P, Qie L. Improving remote sensing of aerosol microphysical properties by near-infrared polarimetric measurements over vegetated land: information content analysis. J Geophys Res Atmos 2018;123:2215–43.
[80] Rodgers CD. Inverse methods for atmospheric sounding: theory and practice. Singapore: World Scientific; 2000.
[81] Jeong U, Kim J, Ahn C, Torres O, Liu X, Bhartia PK, et al. An optimal-estimation-based aerosol retrieval algorithm using OMI near-UV observations. Atmos Chem Phys 2016;16:177–93.
[82] Wu L, Hasekamp O, van Diedenhoven B, Cairns B. Aerosol retrieval from multiangle, multispectral photopolarimetric measurements: importance of spectral range and angular resolution. Atmos Meas Tech 2015;8:2625–38.
[83] Byrd R, Lu P, Nocedal J, Zhu C. A limited memory algorithm for bound constrained optimization. SIAM J Sci Comput 1995;16:1190–208.
[84] Yu J, Li M, Wang Y, He G. A decomposition method for large-scale box constrained optimization. Appl Math Comput 2014;231:9–15.
[85] Sun L, He G, Wang Y, Fang L. An active set quasi-Newton method with projected search for bound constrained minimization. Comput Math Appl 2009;58:161–70.
[86] Sun L, He G, Wang Y, Zhou C. An accurate active set newton algorithm for large scale bound constrained optimization. Appl Math 2011;56:297–314.
[87] Hasekamp OP, Landgraf J. Retrieval of aerosol properties over the ocean from multispectral single-viewing-angle measurements of intensity and polariza-

tion: Retrieval approach, information content, and sensitivity study. J Geophys Res 2005;110:D04203.
[88] Holzer-Popp T, Schroedter-Homscheidt M, Breitkreuz H, Martynenko D, Klüser L. Improvements of synergetic aerosol retrieval for ENVISAT. Atmos Chem Phys 2008;8:7651–72.
[89] Frankenberg C, Hasekamp O, O'Dell C, Sanghavi S, Butz A, Worden J. Aerosol information content analysis of multi-angle high spectral resolution measurements and its benefit for high accuracy greenhouse gas retrievals. Atmos Meas Tech 2012;5:1809–21.
[90] Jacob DJ. Lectures on inversion modeling. Harvard University; 2007.
[91] Li Z, Xu H, Li K, Li D, Xie Y, Li L, et al. Comprehensive study of optical, physical, chemical and radiative properties of total columnar atmospheric aerosols over China: An overview of Sun-sky radiometer Observation NETwork (SONET) measurements. Bull Am Meteorol Soc 2018;99:739–55.
[92] Ma Y, Li Z, Li Z, Xie Y, Fu Q, Li D, et al. Validation of MODIS aerosol optical depth retrieval over mountains in Central China based on a Sun-sky radiometer site of SONET. Remote Sens 2016;8:111.
[93] Xu H, Li Z, Li D, Li L, Chen X, Xie Y, et al. Ground-based polarimetric remote sensing of dust aerosol properties in Chinese deserts near Hexi Corridor. Adv Meteorol 2014;2014:1–10.
[94] Xie Y, Li Z, Li D, Xu H, Li K. Aerosol optical and microphysical properties of four typical sites of SONET in China based on remote sensing measurements. Remote Sens 2015;7:9928–53.
[95] Dubovik O, Smirnov A, Holben BN, King MD, Kaufman YJ, Eck TF, et al. Accuracy assessments of aerosol optical properties retrieved from Aerosol Robotic Network (AERONET) Sun and sky radiance measurements. J Geophys Res 2000;105:9791–806.
[96] Kokaly RF, Clark RN, Swayze GA, Livo KE, Hoefen TM, Pearson NC, et al.. USGS spectral library version 7. Data series. Reston, VA: USGS; 2017. p. 68.
[97] Baldridge AM, Hook SJ, Grove CI, Rivera G. The ASTER spectral library version 2.0. Remote Sens Environ 2009;113:711–15.
[98] von Hoyningen-Huene W, Freitag M, Burrows JB. Retrieval of aerosol optical thickness over land surfaces from top-of-atmosphere radiance. J Geophys Res Atmos 2003;108:4260.
[99] von Hoyningen-Huene W, Kokhanovsky AA, Burrows JP, Bruniquel-Pinel V, Regner P, Baret F. Simultaneous determination of aerosol- and surface characteristics from top-of-atmosphere reflectance using MERIS on board of ENVISAT. Adv Space Res 2006;37:2172–7.
[100] Litvinov P, Hasekamp O, Cairns B, Mishchenko M. Reflection models for soil and vegetation surfaces from multiple-viewing angle photopolarimetric measurements. J Quant Spectrosc Radiat 2010;111:529–39.
[101] Litvinov P, Hasekamp O, Dubovik O, Cairns B. Model for land surface reflectance treatment: physical derivation, application for bare soil and evaluation on airborne and satellite measurements. J Quant Spectrosc Radiat 2012;113:2023–39.
[102] Clark RN, Swayze GA, Wise R, Livo E, Hoefen T, Kokaly R, et al. USGS digital spectral library splib06a: U.S. Geological Survey, Digital Data Series 231 http://speclab.cr.usgs.gov/spectral.lib06.
[103] Strahler AH, Muller J-P. MODIS Science Team Members. MODIS BRDF/Albedo Product: Algorithm Theoretical Basis Document Version 5.0. MODIS Documentation. Boston, MA, USA: Boston University; 1999.
[104] Qie L, Li Z, Sun X, Sun B, Li D, Liu Z, et al. Improving remote sensing of aerosol optical depth over land by polarimetric measurements at 1640 nm: airborne test in North China. Remote Sens 2015;7:6240–56.
[105] Wang H, Yang L, Deng A, Du W, Liu P, Sun X. Remote sensing of aerosol optical depth using an airborne polarimeter over North China. Remote Sens 2017;9:979.
[106] Hou W, Li Z, Zheng F, Qie L. Retrieval of aerosol microphysical properties based on the optimal estimation method: Information content analysis for satellite polarimetric remote sensing measurements. In: Proceedings of the international archived of the photogrammetry, remote sensing and spatial information sciences, ISPRS TC III Mid-term symposium "development, technologies and applications in remote sensing". Beijing; 2018. p. 533–7.
[107] Xu F, van Harten G, Diner DJ, Kalashnikova OV, Seidel FC, Bruegge CJ, et al. Coupled retrieval of aerosol properties and land surface reflection using the airborne multiangle SpectroPolarimetric imager. J Geophys Res Atmos 2017;122:7004–26.
[108] Xu F, Dubovik O, Zhai P-W, Diner DJ, Kalashnikova OV, Seidel FC, et al. Joint retrieval of aerosol and water-leaving radiance from multispectral, multiangular and polarimetric measurements over ocean. Atmos Meas Tech 2016;9:2877–907.
[109] Manolis I, Grabarnik S, Caron J, Bézy J-L, Loiselet M, Betto M, et al.. The metop second generation 3MI instrument. SPIE Remote Sensing: SPIE; 2013. p. 13.
[110] Manolis I, Bézy J-L, Meynart R, Porciani M, Loiselet M, Mason G, et al. The 3MI instrument on the MetOp second generation. In: Proceedings of the international conference on space optics — ICSO 2014. SPIE; 2017. p. 9.
[111] Marbach T, Riedi J, Lacan A, Schlüssel P. The 3MI mission: multi-viewing-channel-polarisation imager of the EUMETSAT polar system: second generation (EPS-SG) dedicated to aerosol and cloud monitoring. SPIE Optical Engineering + Applications: SPIE; 2015. p. 8.
[112] Mishchenko MI, Cairns B, Hansen JE, Travis LD, Kopp G, Schueler CF, et al. accurate monitoring of terrestrial aerosols and total solar irradiance: introducing the glory mission. Bull Am Meteorol Soc 2007;88:677–91.
[113] EUMETSAT. The atmospheric motion vector retrieval scheme for meteosat second generation. Lome, Australia: Proc Fifth Int Winds Workshop; 2000.
[114] Schmetz J, Pili P, Tjemkes S, Just D, Kerkmann J, Rota S, et al. An introduction to Meteosat second generation (MSG). Bull Am Meteorol Soc 2002;83:977–92.
[115] Dubovik O, King MD. A flexible inversion algorithm for retrieval of aerosol optical properties from Sun and sky radiance measurements. J Geophys Res Atmos 2000;105:20673–96.
[116] Zhang Y, Li Z, Zhang Y, Li D, Qie L, Che H, et al. Estimation of aerosol complex refractive indices for both fine and coarse modes simultaneously based on AERONET remote sensing products. Atmos Meas Tech 2017;10:3203–13.